Searching for distant galaxy clusters in the XMM-XXL southern field using deep z-band images from DECam

Author:
David Brinson Gardner

Supervisors:
Dr. Lee Spitler
Dr. Chris Lidman
Dr. Matt Owers

A thesis submitted to Macquarie University
for the degree of Master of Research
Department of Physics and Astronomy
February 2015

Typeset in LaTeX 2_ε.

Except where acknowledged in the customary manner, the material presented in this thesis is, to the best of my knowledge, original and has not been submitted in whole or part for a degree in any university.

David Brinson Gardner

Acknowledgements

I would like to thank my co-supervisor, Chris Lidman, for conceiving the project and acquiring all of the DECam data used. Thanks also to my other co-supervisor, Matt Owers, for his invaluable assistance with IDL and for making it possible for me to show my work to the XXL consortium. And thanks to my supervisor, Lee Spitler, for guidance throughout the year, particularly at the beginning and end when I needed it most. I would also like to thank the AAO for assisting in sending me to Chile to observe using DECam on the Blanco 4 m telescope, where we were unfortunately clouded out. Thanks to Bruno Altieri for discussions and guidance during the observing run in Chile. A big thank you to Shantanu Desai for all of his help in understanding the data reduction process and for travel advice in Germany. Thanks to the Marguerite Pierre and all of the XXL consortium for their invitation and gracious welcome in Italy at the consortium meeting. Thanks also to Andrew DeGroot for providing the cluster finding algorithm as well as his guidance when updating the algorithm. Thanks to the Department of Physics and Astronomy at Macquarie University for all of their support throughout my degree. Thanks also to all of the astronomy students and post docs for their discussions and assistance throughout the year. A very special thanks to Amanda for putting up with me this year and being an extraordinary copy editor. Finally, thanks to Xena for always being a welcome distraction when tennis balls were needing to be chased.

Abstract

We present a high-redshift galaxy cluster candidate catalogue created using two galaxy based detection methods: z' and 3.6 μm red sequence method and the Stellar Bump Sequence method. This utilises new z' band observations from the dark energy camera on the 8 m Blanco telescope in CTIO, Chile, in addition to mid-infrared Spitzer observations from the SSDF survey. These observations have 5σ sensitivity limits of 24.4, 21.8 and 21.5 AB magnitude in z', 3.6 μm and 4.5 μm bands respectively. We create an aperture corrected z' band catalogue which is cross-referenced with an existing aperture corrected Spitzer 3.6 μm and 4.5 μm catalogue, to produce a catalogue containing 2,137,515 unique objects in the XXL-S field. We then use custom redshifted BC03 stellar population models to simulate the galactic red sequence, that we use to match observed colours created from the three bands used. By assigning redshifts based on colours to objects in our catalogue, we are able to create a spatial density map which we then analyse to look for overdensities of galaxies. Finally, we present a catalogue that contains 802 candidate galaxy clusters in the redshift range $0.4 < z < 2.1$, of which 721 are new detections. We also detect 32 spectroscopically confirmed X-ray selected galaxy clusters at redshifts up to $z = 0.87$

Contents

1 Introduction

1.1 Clustering of galaxies

Early observations by William Herschel and Charles Messier revealed that nebulae had an affinity for clustering together. Hubble (1926) revolutionised the study of these clustering nebulae when he discovered that elliptical and spiral nebulae were extra-galactic, and were actually independent galaxies similar to our own Milky Way Galaxy. This discovery revealed that these clusters of nebulae, now known to be galaxy clusters, are enormous in size and at the present epoch are the largest and most massive virialised objects in the universe.

The hierarchical model of structure formation, which is the currently accepted paradigm explaining structure formation, suggests that objects are formed through mergers and accretions of smaller systems (Kravtsov & Borgani 2012). Galaxy clusters, and clusters of clusters, are the largest structures currently formed through this model. Density perturbations in the primordial universe collapse to form subgalactic objects which then combine to form galaxies that finally collect into galaxy clusters (Voit 2005). However, there are observational constraints on the early formation of large-scale structures, because of the paucity of known clusters at $z > 1.5$ (when the universe was 4.3 Gyr old). The limited $z > 1.5$ galaxy clusters that have been studied to date provide some interesting clues about their formation

and impact on galaxy formation. Unfortunately, due to small numbers, the observational results are inconclusive and even contradictory at times.

For instance, some studies of high-redshift galaxy clusters have revealed that galactic evolution is accelerated as galaxy number density increases, especially in cluster cores (Tran et al. 2010; Grützbauch et al. 2012). Galaxy clusters are regions of very high density, but they also show increased number density in their cores. In the local universe, cluster cores are home to some of the most massive galaxies in the universe, which also appear to be the oldest. Galaxies that are in the cluster core generally appear to age much faster than other cluster galaxies, and all cluster members appear older than field galaxies at the same redshift (Grützbauch et al. 2012).

This is supported by Grützbauch et al. (2012) whose observations of galaxies in the core of cluster XMMU J2235.3-2557, at redshift $z = 1.4$, show that the star formation rate (SFR) is very low, and in some galaxies has turned off completely. As in most clusters at lower redshifts, galaxies within ~ 200 kpc of the cluster centre show low levels of star formation. Grützbauch et al. (2012) propose that this is the quenching radius at which star formation is turned off, possibly due to either interactions with the intracluster medium (ICM) or interactions with other galaxies in the dense cluster core.

Conversely, Hilton et al. (2010) report that the galaxy cluster XMMXCS J2215.9-1738, at $z = 1.46$, appears to have multiple galaxies located in its core with high SFRs. Tran et al. (2010) demonstrate similar findings in the galaxy cluster CIG J0218.3-0510, at $z = 1.6$, which has a large increase in star formation with increasing density. Both of these papers show opposite trends to what Grützbauch et al. (2012) found at a similar redshift. Tran et al. (2010) concludes that CIG J0218.3-0510 will have its high SFR quenched rapidly and that this epoch is when galaxies in clusters are still very active.

As these studies have shown, further research is required to increase our understanding of how a galaxy's environment affects its evolution. The pivotal point in evolution of galaxy clusters appears between redshifts $1.3 < z < 1.6$ during which mechanisms driving star formation shut down in the core galaxies. To further understand the processes involved in driving galaxy evolution, we need a larger sample of high-redshift galaxy clusters. The past decade has marked a significant increase in effort to using multi-wavelength techniques to search for galaxy clusters and the amount of spectroscopically confirmed clusters at $z > 1$ has increased from only a few to ~ 100. Further work is still required for a more representative high-redshift cluster catalogue as the number of confirmed clusters at $z > 1.4$ is only now > 10 (Muzzin et al. 2013; Newman et al. 2014).

1.2 Detecting galaxy clusters using different wavelengths

This section will outline the three major techniques currently used to detect galaxy clusters at redshifts $z > 1.5$; X-ray observations of hot intracluster gas, millimetre observations of scattered cosmic microwave background photons and the detection of galaxies through infrared observations.

1.2.1 X-ray emission of hot intracluster gas

Voit (2005) states that galaxy formation is extremely inefficient as $\sim 90\%$ of the baryons in the universe never collapsed to form stars and instead largely reside in the intergalactic voids as baryonic gas. Massive galaxy clusters form large potential wells which collect and gravitationally compress this intergalactic gas, heating it to X-ray emitting temperatures ($\sim 10^8\,\mathrm{K}$). This super-heated gas is detected as an extended X-ray source that can be used to infer the cluster mass as the amount of heating is directly related to the mass of the cluster (i.e. depth of potential well). That is, baryons in the potential wells of more massive clusters are heated more than those in less massive clusters.

As redshift increases, galaxy cluster detection from X-ray emission becomes more difficult due to a decrease in photons arriving at our detectors. This decrease is due to the combination of distance and cosmological expansion, which causes the surface brightness of an object to decrease as $(1 + z)^4$. This loss of flux necessitates ever increasing integration times to enable detection of more distant clusters. As these detections can only be made from space-based telescopes, research in this area becomes more expensive and competitive as longer observations are required.

These high-redshift X-ray clusters are also difficult to detect as, predicted by the hierarchical model, they have had less time to accumulate mass. As previously mentioned, the mass of a cluster is the driving force behind X-ray emission. These less massive clusters are less luminous in the X-ray spectrum, which further increases the problem of detecting photons and requires even longer integration times.

Furthermore, detecting X-ray clusters is susceptible to contamination by active galactic nuclei (AGN). This is the result of X-ray AGN emission dominating at faint flux levels. The resolution of XMM is too poor to discriminate between a distant cluster and an AGN, so AGNs can contaminate distant cluster samples.

1.2.2 Scattering of cosmic microwave background photons

The hot baryonic gas in the ICM is also indirectly visible at millimetre wavelengths. As cosmic microwave background (CMB) photons pass through the hot ICM, $\sim 1\%$ are inverse compton scattered (Bleem et al. 2014b) to higher energies. This effect, known as the Sunyaev-Zel'dovich effect (SZE; Sunyaev & Zeldovich 1972), creates a measurable change in the CMB spectrum, and is highly dependent on the mass of a cluster.

This mass dependence is due to the change detected from the SZE and is proportional to the ICM pressure integrated along the line of sight. The pressure of the ICM, which is in hydrostatic equilibrium with the cluster potential, depends on the size of cluster's gravitational potential well. This mass dependence makes it harder to detect younger, less massive clusters that will typically be located at high-redshifts.

The hierarchical model of structure formation dictates that the cluster mass will be lower at higher redshifts. This means that the resulting SZE is potentially difficult to detect at high-redshifts, although four $z \geq 1.5$ cluster candidates have recently been reported by Bleem et al. (2014b). The advantage of this method is that, unlike X-ray detections, SZE detections do not suffer from surface brightness dimming, which decreases as $(1 + z)^4$.

1.2.3 Infrared emission from cluster galaxies

Unlike the X-ray and millimetre methods, infrared (IR) observations are used to detect clusters by imaging stellar light from cluster galaxies.

As redshift increases, observations become increasingly difficult at optical wavelengths due to the bulk of emission shifting to the near-IR. This forces observations of high-redshift galaxies to space-based telescopes, which are expensive and access is highly competitive.

Core galaxies are the most massive and therefore brightest galaxies, the brightest of which is called the brightest cluster galaxy (BCG). BCGs at the current epoch are some of the most luminous and massive galaxies in the universe (Lidman et al. 2012). When pushing to redshifts of $z > 1.5$, these cluster core galaxies are the easiest to detect due to their increased brightness when compared to non-core cluster members.

Detecting galaxy clusters with IR surveys is susceptible to erroneously including line of sight galaxies in cluster samples, as this method is sensitive to projection effects. To try and prevent contamination from non-cluster galaxies, a multi-wavelength approach is commonly used to photometrically determine the rough redshift of potential cluster members. This is accomplished by comparing redshifted stellar population models to colours created using observations from different wavelength bands. These colours are especially useful in detecting clusters as cluster galaxies are typically older and much redder than field galaxies at the same

redshift (Voit 2005). This means they have strong spectral breaks, which can be identified relatively inexpensively with broadband imaging in multiple filters. It is it important to note that at redshifts $z > 1.6$, the difference in field to cluster galaxy colours is not as significant as in the low-redshift neighbourhood, as reported by (Tran et al. 2010).

1.3 Galaxy cluster detection using observations in the near infrared

Early-type galaxies follow a distinct locus in colour-magnitude space with typical scatter of 0.05 magnitudes (Bower et al. 1992). This colour-magnitude relation is known as the red sequence and can be used as an indicator of redshift (Gladders & Yee 2000). Even though cluster galaxies appear to have a high SFR at redshifts $z > 1.6$, Spitler et al. (2012) finds that the red sequence is still visible in cluster galaxies at $z > 2$. It was also demonstrated by Gladders & Yee (2000) that the red sequence of cluster galaxies could be detected using only two photometric bands. Muzzin et al. (2009) and Wilson et al. (2009) adapted this technique into the mid-infrared (MIR) and galaxy clusters up to $z \sim 1.4$ were detected using z' band ($\sim 9000\,\text{Å}$) and $3.6\,\mu$m observations. While this method was able to detect clusters at redshifts higher than that proposed by Gladders & Yee (2000), deep observations were required for the optical z' band component.

Papovich (2008) proposed a method for detecting clusters using only MIR data as he demonstrated that high-redshift galaxies have red $3.6\,\mu$m - $4.5\,\mu$m colours and even distant galaxies are bright enough to be detected at these wavelengths. Muzzin et al. (2013) presented a modified version of the method proposed by Papovich (2008) as a two-colour, three-band method that combines photometry from z' band, $3.6\,\mu$m and $4.5\,\mu$m observations.

This new method is able to remove low-redshift interlopers using the z' band observations and is also able to push to high redshifts using the $3.6\,\mu$m and $4.5\,\mu$m data. Muzzin et al. (2013) found a galaxy cluster at $z = 1.63$, which has been spectroscopically confirmed, using their new method known as the Stellar Bump Sequence (SBS).

1.4 This study

This thesis outlines all processes involved in creating a high-redshift galaxy cluster candidate catalogue using two photometric techniques: z' and $3.6\,\mu$m red sequence method proposed by Muzzin et al. (2009) and the SBS method presented by Muzzin et al. (2013). We improve on previous work by Muzzin et al. (2013) by using deeper z' band data which enables us to

push to higher redshifts. This study will focus on a 25 square degree region in the southern sky, known as XXL-S (discussed in Chapter 2), within the redshift range $0.4 < z < 2.1$. The predicted number of galaxy clusters containing $> 10^{14}$ solar masses within the volume analysed by this study is 115, using the halo mass function as described by Tinker et al. (2008). We are also able to compare our catalogue with other catalogues as we have chosen to search in an area that has extensive coverage in the X-rays and in the submillimeter. We start by describing the observations performed for data acquisition and then focus on all steps conducted to create photometric source catalogues in Chapter 2. Chapter 3 outlines the two methods in detail and their application in the detection of galaxy cluster candidates. We then present our results and analysis in Chapter 4 and include our full candidate cluster catalogue in Appendix A. Our conclusion, in Chapter 5, discusses the possibilities for expansion of this research in future studies.

2

Image Analysis

This chapter will cover how and where the observations were made, methods employed to produce science ready images from the observations, all steps leading to the creation of the final cross-matched catalogues and final astrometric comparisons between data sources.

2.1 XXL fields

The z' band observations made for this project form part of the XXL survey. XXL is primarily an X-ray survey which aims to provide constraints on the dark energy equation of state (Pierre et al., in preparation). XXL aims to achieve this goal by providing a well-defined sample of X-ray selected galaxy clusters at redshifts $z < 1$. There are also associated multi-wavelength programs to increase the science potential of the X-ray observations, including the observations which form part of our study.

XXL consists of two 25 square degree fields; the northern (XXL-N) field centred at 2h20 -5d00 and the southern (XXL-S) field at 23h30 -55d00. Several factors had to be considered when choosing these two locations.

Firstly, X-rays are attenuated by intervening gas associated within our galaxy, therefore it is best to choose regions with low column densities of foreground galactic gas. The low foreground is also beneficial to the multi-wavelength follow-up observations. These fields

were also required to be visible to XMM as well as the ESO telescopes used in the associated multi-wavelength programs. The choice to split XXL in to two fields reduces cosmic variance without compromising the ability to probe large scale structure. Splitting the fields also has the added benefit of making observations easier to schedule. The final choice in fields takes advantage of the existing XMM observations in both fields as well as optical coverage in XXL-S from the Blanco cosmology survey.

2.2 z' band data reduction from the dark energy camera

The Stellar Bump Sequence (SBS), one of our detection methods, uses two colours (three bands) to identify galaxy clustering at high-redshifts. The SBS algorithm employs optical (z' band) and mid-infrared (3.6 μm and 4.5 μm) data to determine redshifts photometrically. Our other method, which is a modified red sequence method, requires only the z' band and 3.6 μm data for photometric redshift estimations. To obtain optically deep XXL-S data in the z' band, observations were required using the dark energy camera on the Blanco 4 m telescope in Chile. The z' band observing strategy and data reduction techniques employed are outlined in this section. The mid-infrared data is discussed in Section 2.4.

2.2.1 z' band observations

The dark energy camera (DECam) is a wide-field CCD imager mounted at the prime focus of the Victor M. Blanco 4 m telescope that is located at the Cerro Tololo Inter-American Observatory (CTIO), Chile. DECam is ideal for this project as the CCDs are much more sensitive (a factor of 5-10) in longer wavelengths ($\sim$ 9000 Å - 10000 Å) compared to traditional astronomical CCDs (DePoy et al. 2008). We require observations in z' band (8095 Å - 10268 Å), thus DECam is an ideal instrument to use.

DECam consists of 62 2000 $\times$ 4000 pixel CCDs with a pixel scale of 0.27" per pixel and a focal plane which captures a total area of 3.0 square degrees. This 3.0 square degree field of view enables the entire XXL-S field to be covered with 13 pointings. During our observations, only 60 science CCDs were used as two science CCDs on DECam were damaged.

DECam observations in XXL-S were carried out in July and August, 2013 (P.I. Chris Lidman). Observations were executed in the four $griz'$ bands, with 12 of the 13 planned z' band observations performed. The central locations of these 13 pointings are listed in Table 2.1. At the time of writing, pointing 3 is only partially complete and there are no

observations currently available from pointing 1. The two pointings required to complete the z' band observations were originally planned for 2014, but were not possible due to weather. z' band observations at pointings 1 and 3 are planned for 2015. Figure 2.1 shows the currently observed z' band DECam pointings in red, and green circles represent the previous XMM-Newton pointings. Pointing 1 is located on the left side of Figure 2.1 where there is no overlap with the XMM data.

TABLE 2.1: Pointings for DECam observations in XXL-S. Note: Observations in z' band at pointings 1 and 3 are planned for 2015

Pointing	R.A. deg., J2000	Dec. deg.,J2000
1	357.30	-54.75
2	356.40	-56.25
3	353.55	-52.60
4	353.55	-54.35
5	353.30	-56.25
6	350.55	-52.60
7	349.80	-54.75
8	350.10	-56.25
9	356.10	-53.50
10	355.20	-55.00
11	352.00	-53.50
12	352.00	-55.00
13	348.90	-53.50

Each DECam pointing has a total integration time of 8000 seconds in the z' band from 32 250 second individual exposures. These observations are dithered in a rectangular pattern by half of a CCD in R.A. or Dec. At each dither position we have four 250 second exposures, and this sequence is repeated eight times to achieve the 5σ aperture corrected AB magnitude limit of 24.4. By dithering we are able to expose in the gaps between the CCDs as well as minimise effects from bad pixels.

2.2.2 z' band data reduction

This section will outline the data reduction process as applied to the z' band DECam images. The reduction process converts raw data from the telescope into science ready images for catalogue creation and photometric analysis. Data reduction on the z' band DECam images was performed by Shantanu Desai and the pipelines used are almost identical to that employed in the Blanco cosmology survey (BCS; Desai et al. 2012). This data reduction process consists of two pipelines, one for detrending and another for co-addition of exposures. The

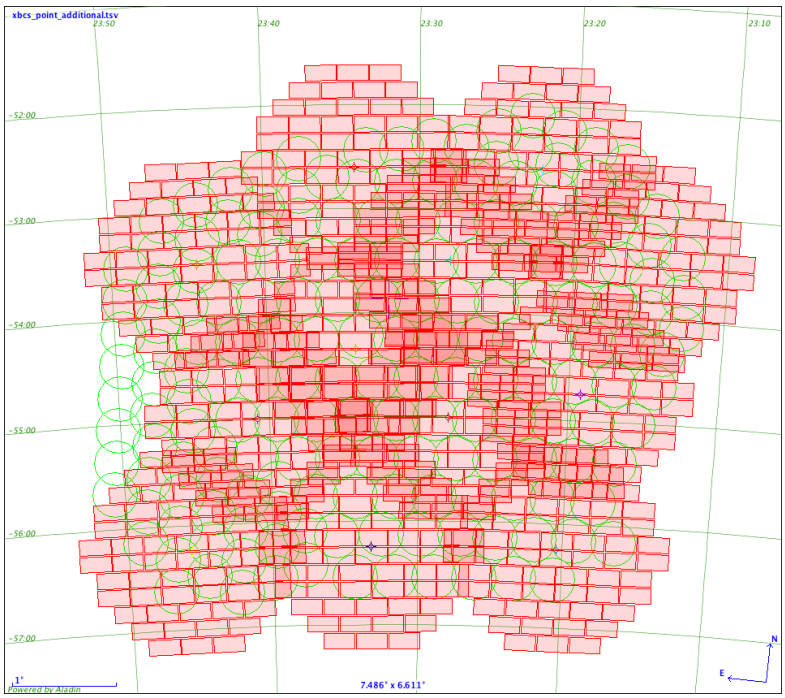

FIGURE 2.1: The current z-band coverage in the XXL-S field. The z-band observations were made using the dark energy camera (DECam) on the Victor M. Blanco 4m telescope at the Cerro Tololo Inter-American Observatory, Chile. The green circles are XMM-Newton pointings in the same field. Shown in red are the 12 DECam pointings. The DECam pointings have a total integration time of 8000 seconds, giving a typical 5σ aperture corrected AB magnitude limit of 24.4.

process of detrending removes instrumental signatures from images and co-addition refers to the combination of multiple exposures from the same part of sky. The detrending pipeline performs cross-talk corrections, overscan correction, bias subtraction, flatfielding, focal plane distortion corrections and astrometric calibration that will be summarised in the following section.

Detrending DECam z' band images

The first step in detrending the images is the removal of cross-talk contamination present in the DECam images. This cross-talk contamination is the largely unavoidable result of having multiple readout amplifiers in multi-CCD imagers. When multiple amplifiers are used to simultaneously read out data from multiple CCDs, a cross-talk signal is induced resulting in ghost images from other CCDs (or other quadrants of the same CCD) appearing in parts of the readout (Freyhammer et al. 2001). The cross-talk coefficients used to remove contamination were estimated by K. Paech (Ludwig Maximilian University of Munich; LMU) using special DECam exposures during DES science verification. One feature of DECam is

that crosstalk between certain ampliers is negative and also requires non-linear crosstalk corrections.

A bias offset is added to the CCD signal to ensure that the readout values are always positive and possesses an intrinsic noise. CCD bias is removed from each exposure by subtracting a bias frame and performing an overscan correction. Bias frames (zero second exposure) are created in the afternoon prior to each nights observations. A bias frame is created to remove bias which varies predictably from pixel to pixel. The overscan offset, however is not predictable. Pseudo pixels, known as overscan strips, are located on two edges of the DECam CCD sensors and are not sensitive to light. The overscan strips are used to detect the bias offset, which varies for each exposure. The bias frames and overscan values are then subtracted from the science data to remove the bias offset applied to the CCDs. These overscan strips are then trimmed from the observational data.

To ensure that the observed data is photometrically calibrated across the image, flat-fielding must be performed. This is required as CCD sensitivity is not uniform across its surface. A flat-field is created by exposing a flat illumination field. After removing the bias offset information, the flat-field will only contain information about pixel-to-pixel sensitivity differences in the CCDs. These flat-field images are then used to scale the image data to remove any variations present.

The Blanco 4 m telescope has a large focal plane which results in the pixel scale varying by about 1% over the field. This variation in pixel scale has an effect on the pixel brightness as a function of position. Desai et al. (2012) opted to correct for this variation by correcting for the pixel response as a function of position in each CCD. This has been applied to DECam for each of the 60 viable science CCDs present. While a flat-field-like image corrects for the variation in pixel sensitivities, this scaling only acts on the source fluxes and does not affect the flat-corrected sky.

Astrometric calibration is the final step in detrending. There are three sources of error in how locations on the sky are mapped to pixels in the image: pointing errors in the telescope, instrumental distortions from large focal plane instruments and, depending on the direction of the pointing, atmospheric refraction. Desai et al. (2012) used the SCAMP (Bertin 2006) software package to model these three sources of astrometric error. SCAMP uses the tangent plane projection model which employs a polynomial expansion to accurately map pixel coordinates to the tangent plane using the 2MASS (Skrutskie et al. 2006) catalogue as a reference. The astrometric corrections are then written to the image headers which will later be required for the co-addition process.

Image co-addition and photometric calibration

All of the overlapping detrended exposures are combined into a single science image in a process called co-addition. Care must be taken with co-addition as the data being combined can be influenced by different observing conditions. The co-addition pipeline entails relative photometric calibration, point-spread-function (PSF) homogenisation, co-adding the images together and then absolute photometric calibration.

Our DECam observations do not uniformly cover the entire field in the four bands ($griz'$) used. This has led to photometric calibration being performed using the full 25 square degree data, instead of the tile-by-tile basis used in BCS.

Relative photometric calibration ensures that each image will correctly represent the relative flux of each object. This calibration involves finding the relative zero-points using stars across the entire field. These stellar objects are then selected using the source extractor (SExtractor; Bertin & Arnouts 1996) morphological output parameter `spread_model`. The relative zero-points for each exposure are then computed using a least squares fit based on all stars analysed across the field. The zero-points are required when co-adding the exposures into one image to ensure preservation of internal photometric calibration.

A PSF in a co-added image can vary greatly across an image, especially if the original exposures contain variable seeing. To ensure that all PSFs are uniform across an image, PSF homogenisation is required. The first step in PSF Homogenisation is modelling the average stellar PSF with PSF Extractor (PSFEx; Bertin 2011) for each exposure. These models are then utilised in the selection of parameters for the target PSF of a tile. A position dependent homogenisation kernel is then created using the selected parameters which is then convolved with all images in a tile. This convolution will bring all images in a tile to a common PSF. All images which contained a PSF FWHM > 1.6" are removed prior to homogenisation to ensure that only the observations with the best seeing are used. The homogenised images are then combined using SWarp (Bertin et al. 2002) to create 14000×14000 pixel co-add tiles.

The importance of homogenisation is illustrated in Figure 2.2 where the difference in magnitudes of two apertures (10px and 12px) is plotted against the magnitude of the 12px aperture. As stellar PSFs should be uniform across the tile, a selection of stellar objects was made to inspect any PSF variance present. A non-homogenised DECam tile is shown in the top of Figure 2.2. This shows a spread of ~ 0.01 magnitude in the magnitude differences of stellar objects. This spread is due to the PSFs varying in size across the tile as a result of observations being made with different seeing conditions. The two plots in the bottom of Figure 2.2 show the same observations after homogenisation was carried out on the individual

exposures. A factor of 10 increase in PSF uniformity was achieved through homogenisation as the spread here is only ~ 0.003 magnitudes.

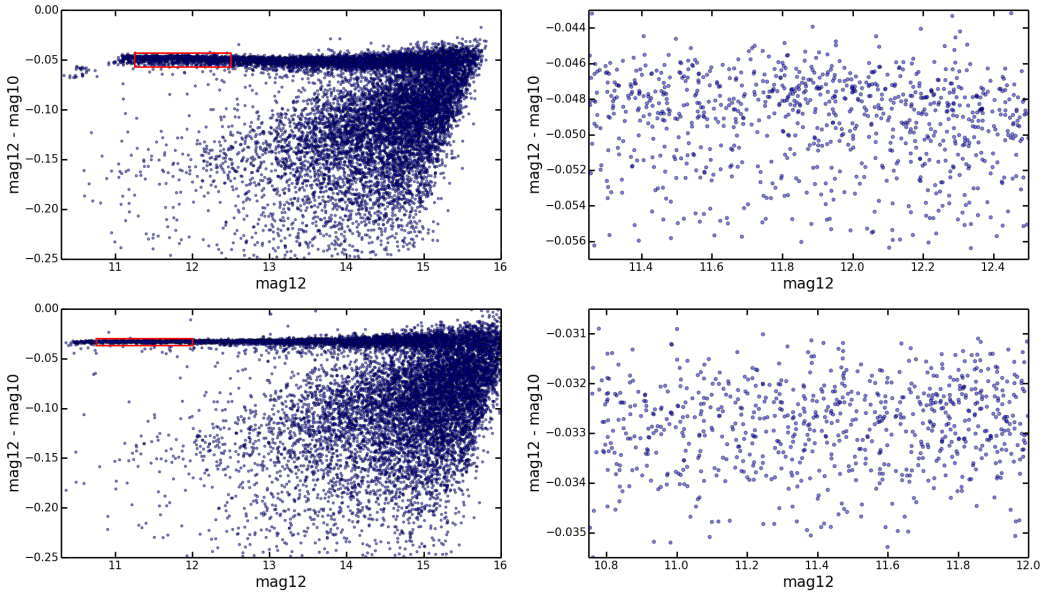

FIGURE 2.2: The effect of PSF homogenisation on the accuracy of aperture magnitudes. The plots show the offset between the magnitude measured in a 12 pixel diameter aperture and a 10 pixel diameter aperture (labelled as mag12 and mag10 in the plots). The top row is the difference of magnitudes before homoginisation and the bottom row is after. The boxes drawn in the left images highlight a region of stellar objects that are examined on the right. The two right images show a zoomed in plot of the highlighted regions. The spread in mag12-mag10 decreases by an order of magnitude from the unhomogenised to homogenised images.

Absolute photometric calibration is the final step in creating a science ready image. This ensures that the photometry in an image is true to the sources on sky. Stellar locus regression (High et al. 2009) is the calibration method used on the DECam observations. Stellar locus regression utilised the observed property that, in colour-colour space, the stellar main sequence follows a pre-determined line. This line is known as the stellar locus and is invariant on the sky. Stellar objects are again selected from the co-adds using the SExtractor `spread_model` parameter. Two fits are then performed on the selected stars using stellar loci from different colour-colour relations. These stellar loci are calibrated using the dark energy survey stellar locus which was empirically determined by K. Paech (LMU). The first fit calibrates the stellar colours and the second fit adjusts the scale by finding the absolute zero point magnitude. After the photometric calibration is complete, the coadds are ready to be used in the creation of source catalogues. The left image in Figure 2.3 shows one of

the science ready z' band DECam coadds.

2.3 z' band source extraction and photometry

This section will outline how the z' band catalogue was created. The z' band observations consist of a $25\,\mathrm{deg}^2$ area with a 5σ aperture corrected AB magnitude limit of 24.4. This results in tiles that contain hundreds of thousands of objects which need to be detected and characterised. SExtractor (Bertin & Arnouts 1996) is a tool that can quickly detect and extract information (photometry and morphology) about these objects and was used in building catalogues from our observations.

2.3.1 Source extraction of z' band DECam data

SExtractor performs six steps while analysing each image: estimation of the sky background, thresholding, deblending, filtering of the detections, photometry and star/galaxy separation (Bertin & Arnouts 1996). The sky background is estimated (and then subtracted) by applying a median filter to background estimator values in a grid which covers the entire image. Thresholding is used to detect objects by convolving the image with a convolution mask and then using Lutz's one pass algorithm (Lutz 1980) on the convolved image. Deblending is then required as objects near each other may be detected as single objects and need to be separated. All of the detections are then filtered to remove any spurious detections which may be present, especially when using low thresholds or when the local background is high. SExtractor then computes user-specified quantities for each object, and Table 2.2 lists the quantities we specified. Finally, SExtractor classifies each object as either a star or a galaxy through the use of a neural network.

As mentioned previously in this chapter, a dithering pattern was utilised during DECam observations to fill in the gaps between the CCDs. This dithering resulted in the field having an uneven amount of exposure. More noise is present in areas with less exposure, giving less certainty to low threshold detections. An exposure map created by Shantanu Desai during the data reduction gives a weighting value based on exposure time. This exposure map is used as a weight map in SExtractor. Areas in the tile with more exposure have a higher weighting, and will be given a higher preference in source detection. The right image in Figure 2.3 shows the weight map for one of the z' band DECam images in which the darker areas have lower weights. SExtractor ignores all regions in the corresponding image where the weight map has a zero value.

Significant effort was conducted to find the SExtractor settings (shown in Table 2.3)

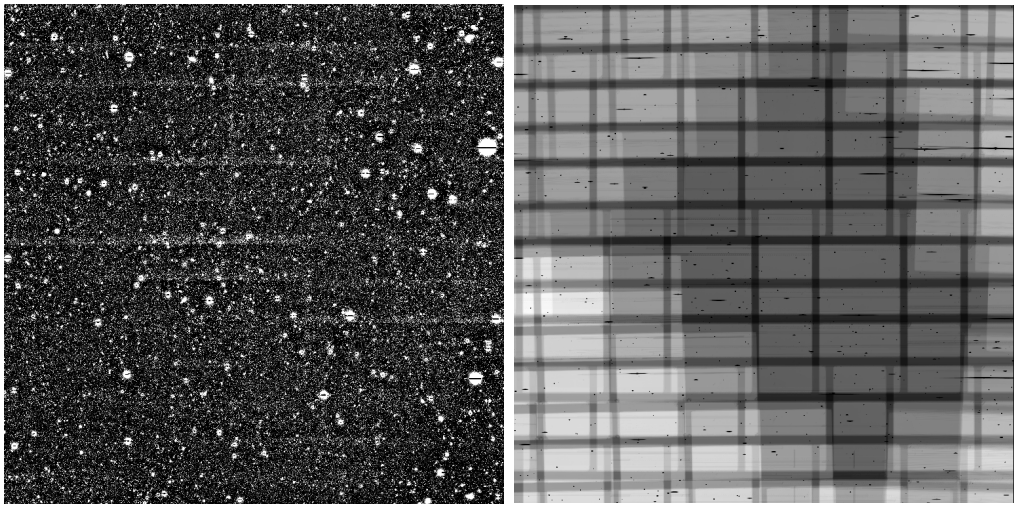

FIGURE 2.3: *Left:* One of the z' band DECam tiles. The noisy regions can be seen in areas with less exposure, especially between the CCD gaps. This 14000×14000 pixel tile is one square degree in size. *Right:* The weight map corresponding to the DECam image on the left. The darker areas have a lower relative weighting value. Masked regions around saturated stars can also be seen as black dots.

we adopted for source extraction of the z' band DECam images; `DETECT_MINAREA` = 5 was used to minimise false detections, `DETECT_THRESH` = 1.0 to maximise the number of objects found, `FILTER` = gauss_3.0_5x5 was chosen to match the seeing, and the rest of the settings in Table 2.3 were empirically found to give the best results. These settings are very similar to those used by the Canada-France-Hawaii Telescope Legacy Survey (Gwyn 2012) with the exception that we require at least five adjacent pixels to be above the detection threshold, compared to their three, to minimise spurious detections. We also used a 10 pixel (2.7") aperture diameter (`PHOT_APERTURES` = 10.0) to measure the magnitude of each source in the z' band data. This aperture size was chosen as it is twice the size of largest seeing FWHM in the DECam z' band images. Figure 2.4 shows a small source extracted region of a z' band tile. The red circles show the objects that were detected in SExtractor using the settings in Table 2.3. The z' band catalogue is created using all sources detected by SExtractor. The aperture photometry reported by SExtractor, however, needs to be corrected to include the flux that falls outside the aperture. The next section outlines this aperture correction process.

2.3.2 Aperture correction of z' band DECam catalogues

The benefit of aperture photometry over measuring the entire flux from an object is that it contains less noise. This is due to the flux of an object being measured where the signal

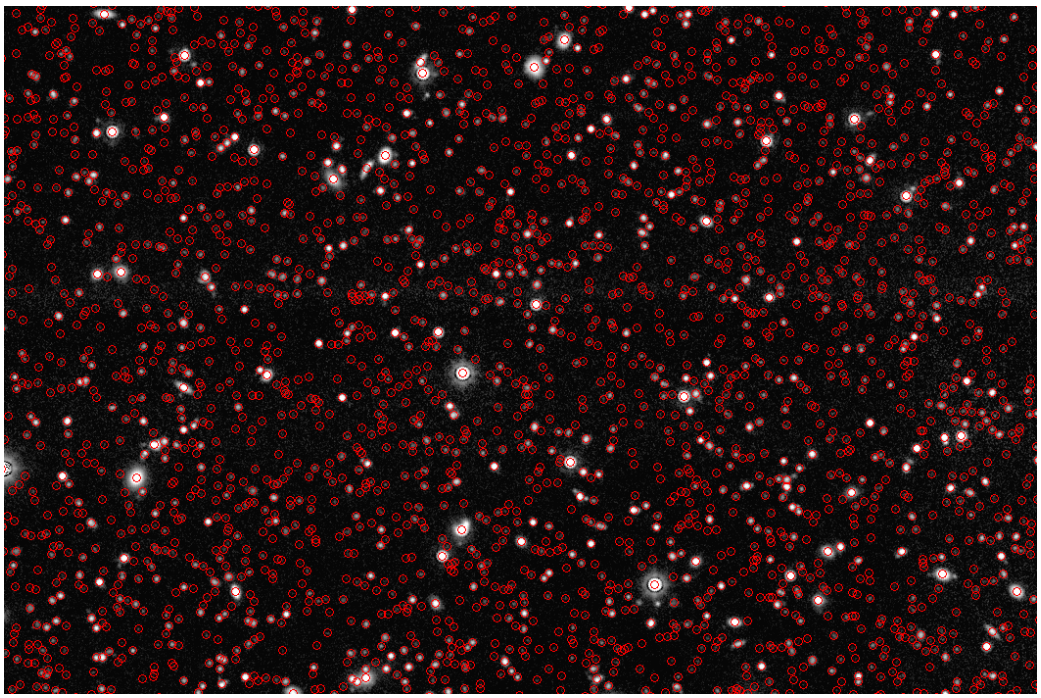

FIGURE 2.4: z' band DECam image with objected detected by SExtractor circled in red.

is much higher than the noise. Aperture photometry, however, does not measure the entire flux as the tails of a PSF fall outside the aperture. To ensure we have the total photometry, the flux that falls outside the aperture needs to be accounted for. We calculate the amount of aperture correction required using stars in each tile as, being point sources, they have a uniform PSF determined by the seeing. For the purpose of our catalogues, we use PSFEx to determine the model PSF for each tile based on stellar sources.

The PSFEx software package determines the model PSF for an image. This PSF is modelled from the stars in an image, which makes it dependent on the seeing conditions when the observations were made. PSFEx finds all point sources in an image and then models the PSF. The model PSF is generated from basis vectors determined by the position the point sources are on a magnitude *vs* half-light-radius stellar locus diagram (Bertin 2011). To prevent aliasing when generating the model PSF, PSFEx resamples the original pixel size. To ensure that the model PSF has the same pixel size as the original image, we set `CHECKIMAGE_TYPE` to `SNAPSHOTS_IMRES`, which writes a FITS file containing the model PSF at the pixel scale of the original image. The left of Figure 2.5 shows a model PSF generated by PSFEx for one of the z' band DECam images and on the right is its radial profile found in IRAF. It is this radial profile that is used to determine the FWHM of the model PSF.

SExtractor was used on the model PSF to determine the amount of flux in two different aperture sizes, 10 pixels and 30 pixels. The aperture correction amount is then calculated

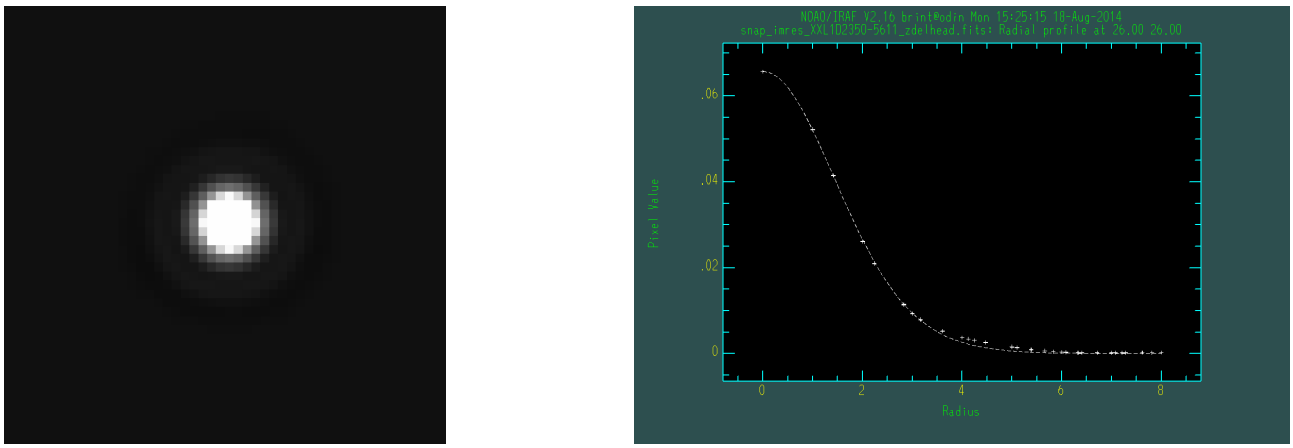

FIGURE 2.5: *Left*: Linear scaling of a model PSF created by PSFEx generated using stellar objects in one of the z' band DECam tiles. The PSF is used to determine the amount of flux neglected when performing aperture photometry. *Right*: Radial profile of the model PSF created using imexamine in IRAF used to measure the PSF FWHM (in pixels).

by subtracting the flux in the larger (30 pixel) aperture from the smaller (10 pixel) aperture. The reminaing flux is what is missed using a 10 pixel aperture. The aperture correction values (listed in Table 2.4) are then added to the 10 pixel aperture magnitudes in the z' band catalogue. It is important to note that we are using stellar generated PSFs to calculate the aperture correction amount to apply to galaxy detections. According to van der Wel et al. (2014), the median half-light radius of a 10^{11} solar mass early-type galaxy at a redshift of $z = 1.0$ is 2.5 kpc, which equates to an angular size of 0.31", assuming a cosmology of $\Omega_\Lambda = 0.7$, $\Omega_m = 0.3$ and $H_0 = 70\,\mathrm{km\,s^{-1}\,Mpc^{-1}}$. As this is much smaller than the average seeing for our z' band observations (1.03"), we chose not to worry about size dependent aperture corrections and assumed the majority of our objects are effectively point-sources on our images.

2.4 Spitzer infrared array camera instrument, images and catalogues

The SBS method requires, in addition to z' band observations (Sections 2.2 and 2.3), mid-infrared (3.6 μm and 4.5 μm) data. The Spitzer Space Telescope was used by Ashby et al. (2013) to perform mid-infrared observations in a region that emcompasses our XXL-S field. Ashby et al. (2013) also created source catalogues from this data, which were used in this study. This section discusses data reduction and catalogue creation using this Spitzer data.

Spitzer was launched by NASA in 2003 with the purpose of observing the universe in

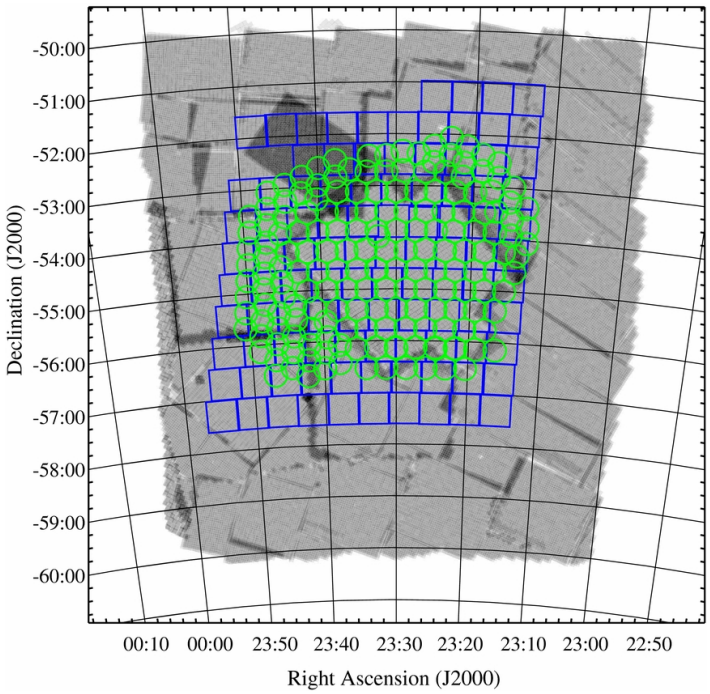

FIGURE 2.6: A Mosaic of the SSDF survey is shown in grey. The green circles are the XMM pointings from the XXL survey. The blue squares are the observations from the Blanco Cosmology Survey. The SSDF observations were carried out in two bands, 3.6 μm and 4.5 μm with 5σ sensitivity limits of 21.8 and 21.5 AB magnitude respectively. (Image source: Ashby et al. 2013)

infrared light. The infrared array camera (IRAC) is a CCD imager and is one of the focal plane instruments on board Spitzer. IRAC is able to make observations in four wavelength bands: 3.6 μm, 4.5 μm, 5.8 μm and 8 μm. The two bands used for this work are 3.6 μm and 4.5 μm.

The data we used is a subset of data from the 94 square degree Spitzer South Pole Telescope Deep Field (SSDF) survey as described in Ashby et al. (2013). Coverage of the SSDF observations is shown in Figure 2.6. The green circles represent the XXL-S XMM pointings and the blue squares are previous observations from the Blanco cosmology survey. Observations in the 3.6 μm and 4.5 μm bands achieved 5σ sensitivity limits of 21.8 and 21.5 AB mag respectively (Ashby et al. 2013). To reach these depths, four 30 second dithered exposures, with an offset of one-third of an IRAC field of view, were required (Ashby et al. 2013).

The data reduction process for the SSDF observations is the same as that used for previous observations in the centre of the SSDF field (PI: S. A. Stanford, PID 40370), with both observations being combined into a single data set (Ashby et al. 2013). As described in Ashby et al. (2013) this was done to ensure that the data had a uniform quality through

the SSDF. The sky was removed by subtracting median-stacked object-masked 3.6 μm and 4.5 μm frames. The sky-subtracted images were then processed using custom software to remove readout effects from bright sources, known as column pulldown effects (Ashby et al. 2013). The images were then mosaicked using IRACproc (Schuster et al. 2006), which is an augmented version of IRAC for use on Spitzer IRAC data. The mosaic was then organised into 46 2×1 square degree tile pairs in both 3.6 μm and 4.5 μm bands. Ashby et al. (2013) then performed astrometry on each pair using the 2MASS catalogue, which created science ready 3.6 μm and 4.5 μm images.

Catalogues were then created with SExtractor using IRACproc generated weight maps. Any pixels which were covered by fewer than 2 exposures were excluded from the detections. Aperture correction was then carried out using empirically determined values and applied to the photometry in the catalogues. SExtractor was run in dual image mode which enabled the detection of objects in one image, a 3.6 μm tile for instance, and photometry to be carried out in both the 3.6 μm and 4.5 μm tiles.

A 2σ 3.6 μm selected aperture corrected SSDF catalogue containing both 3.6 μm and 4.5 μm magnitudes is publicly available through the Astrophysical Journal Supplement Series (Ashby et al. 2013) and was used for this study. The magnitudes in the Spitzer catalogue were converted from the Vega to AB magnitude system by adding 2.788 and 3.255 to the 3.6 μm and 4.5 μm magnitudes respectively.

2.5 DECam and IRAC catalogue cross-matching and astrometry verification

This section will outline the process of cross-matching the DECam and IRAC catalogues to identify all objects which are present in both. Differences between the astrometric systems are also investigated.

2.5.1 Cross-matching DECam and IRAC catalogues

The DECam z' band and IRAC SSDF catalogues are cross-matched to identify all objects that are present in all of the bands. The tool for operations on catalogues and tables (TOPCAT) and starlink tables infrastructure library (STIL; Taylor 2005) software packages were used to create the cross-matched catalogue. We used TOPCAT, which is a graphical frontend for STIL, to cross-match the catalogues and hereafter we will use TOPCAT to refer to both software packages.

TOPCAT is capable of quickly cross-matching very large catalogues and was ideal for this purpose. To give an idea of the cross-matching speed, we were able to match a catalogue from one of the z' band tiles which contained 325,308 entries with the SSDF catalogue which has over 1.6×10^7 entries in less than 30 seconds. TOPCAT is able to match objects based on their angular separation on the celestial sphere. The angular separation between objects is found by comparing the declination and scaled right ascension of each entry in the catalogues. This separation is compared to a user defined maximum allowable error to determine if a match is made. We chose to allow for a 1" maximum angular separation between objects as this was about the size of the average PSF FWHM. In the event that there were multiple matches for the same object, we chose to only accept the objects with the smallest angular separation as being a successful match. The final cross-matched catalogue contains 2,137,515 unique objects.

2.5.2 Verifying the astrometry between the two sets of data

As the data from each instrument was reduced differently, astrometric analysis on the two sets of data is required to ensure that colours created with the cross-matched catalogue are correct.

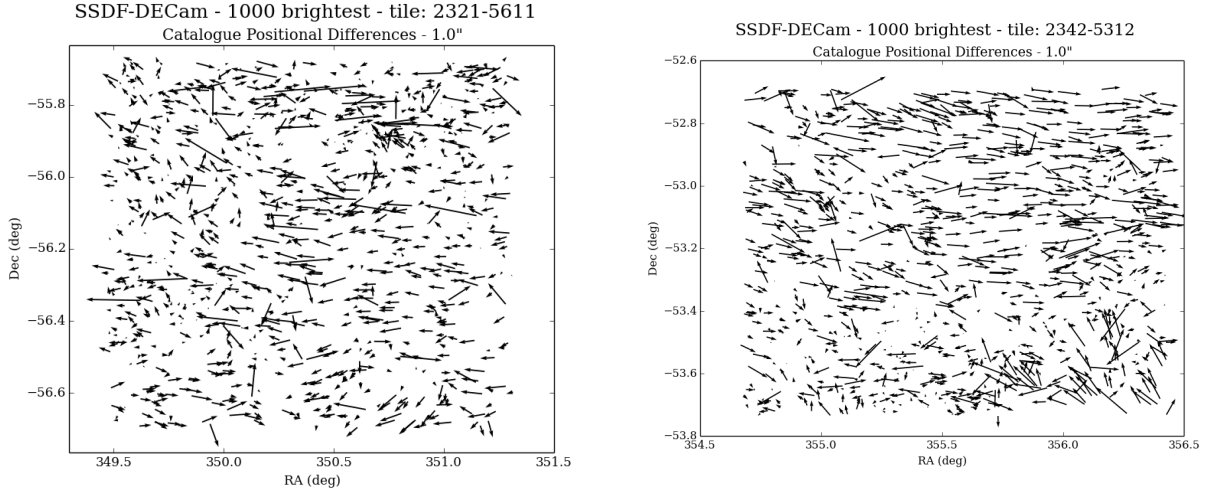

FIGURE 2.7: Quiver plot showing the positional offsets of the 1000 brightest SSDF and DECam objects in two 1 square degree areas of the XXL-S field. The region being plotted is chosen from the boundaries of the z-band DECam tiles. The vectors have been scaled by 100 to help illustrate the offset direction, as indicated by the arrows. *Left*: No preferred offset direction is observed. *Right*: The top half of the plot has a strong bias to the right. This shows that the astrometry is incorrect for the SSDF images as the boundary of the biased vectors are due to the boundary of the Spitzer tile. While there is a discrepancy in the astrometric calibrations between SSDF tiles, the actual offsets are much less than a single PSF and are considered negligible.

Figure 2.7 shows that the direction of the offsets between the two catalogues are largely random. The separation between the two images is shown as a vector, which indicates the direction of the offset. The vectors in both of the plots in Figure 2.7 were scaled by 100 as a visual aid and only the 1000 brightest objects were plotted to make inspection easier. In the top half of the right plot in Figure 2.7, there is a distinct horizontal offset visible. This is due to two IRAC images overlapping in the middle of a single DECam image. We assume this is a result of the IRAC tiles being astrometrically calibrated individually, and not as a single set. There is also an offset visible in the bottom right of the plot. It is important to note that these offsets are much smaller than a single PSF. The images were also stacked to visually inspect the separation with a substantial part of each object overlapping with its match. We concluded that the cross-matched catalogues were adequate and no astrometric correction was required.

TABLE 2.2: The user-specified quantities requested from SExtractor about each detected object

Parameter	Description	Units
NUMBER	Running object number	–
X_IMAGE	Object position along x	pixel
Y_IMAGE	Object position along y	pixel
ALPHA_J2000	Right ascension of barycenter (J2000)	deg
DELTA_J2000	Declination of barycenter (J2000)	deg
KRON_RADIUS	Kron apertures in units of A or B	–
BACKGROUND	Background at centroid position	count
FLUX_RADIUS	Fraction-of-light radii	pixel
ALPHAPEAK_J2000	Right ascension of brightest pix (J2000)	deg
DELTAPEAK_J2000	Declination of brightest pix (J2000)	deg
X2_IMAGE	Variance along x	pixel^2
Y2_IMAGE	Variance along y	pixel^2
XY_IMAGE	Covariance between x and y	pixel^2
A_IMAGE	Profile RMS along major axis	pixel
B_IMAGE	Profile RMS along minor axis	pixel
THETA_IMAGE	Position angle (CCW/x)	deg
A_WORLD	Profile RMS along major axis (world units)	deg
B_WORLD	Profile RMS along minor axis (world units)	deg
THETA_WORLD	Position angle (CCW/world-x)	deg
CLASS_STAR	S/G classifier output	–
FLAGS	Extraction flags	–
MAG_AUTO	Kron-like elliptical aperture magnitude	mag
MAGERR_AUTO	RMS error for AUTO magnitude	mag
MAG_APER	Fixed aperture magnitude vector	mag
MAGERR_APER	RMS error vector for fixed aperture mag.	mag
FLUX_AUTO	Flux within a Kron-like elliptical aperture	count
FLUXERR_AUTO	RMS error for AUTO flux	count
FLUX_APER	Flux vector within fixed circular aperture(s)	count
FLUXERR_APER	RMS error vector for aperture flux(es)	count

TABLE 2.3: SExtractor settings used for creating the z' band DECam catalogue

Parameter	Setting
DETECT_MINAREA (pixel)	5
DETECT_THRESH(sigma)	1.0
FILTER	gauss_3.0_5x5
DEBLEND_NTHRESH	32
DEBLEND_MINCONT	0.005
BACK_SIZE (pixel)	16
BACK_FILTERSIZE	3
BACKPHOTO_TYPE	GLOBAL

Table 2.4: Aperture correction values for the z' band DECam tiles when a 2.7" diameter aperture (10 pixels) is used for photometry. The seeing FWHM is also listed for each tile as calculated by PSFEx.

DECam tile	AC (mag)	seeing FWHM (arcsec)	DECam tile	AC (mag)	seeing FWHM (arcsec)
2308-5412	-0.16	1.15	2335-5113	-0.26	1.34
2309-5213	-0.13	1.09	2335-5213	-0.26	1.34
2309-5312	-0.14	1.10	2335-5312	-0.12	1.06
2313-5710	-0.07	0.92	2335-5412	-0.09	0.98
2314-5511	-0.15	1.14	2335-5511	-0.11	1.03
2314-5611	-0.06	0.90	2335-5611	-0.15	1.14
2315-5312	-0.13	1.08	2335-5710	-0.18	1.19
2315-5412	-0.15	1.15	2341-5113	-0.23	1.30
2316-5113	-0.10	0.98	2341-5213	-0.19	1.19
2316-5213	-0.11	1.00	2342-5312	-0.08	0.95
2321-5511	-0.13	1.08	2342-5412	-0.09	0.97
2321-5611	-0.06	0.90	2342-5511	-0.09	0.97
2321-5710	-0.06	0.90	2342-5611	-0.08	0.95
2322-5113	-0.10	0.99	2343-5710	-0.07	0.92
2322-5213	-0.09	0.98	2348-5213	-0.08	0.95
2322-5312	-0.09	0.98	2348-5312	-0.08	0.95
2322-5412	-0.14	1.12	2349-5412	-0.08	0.96
2328-5312	-0.07	0.93	2349-5511	-0.09	0.97
2328-5412	-0.09	0.98	2350-5611	-0.06	0.90
2328-5511	-0.13	1.08	2350-5710	-0.06	0.91
2328-5611	-0.12	1.06	2355-5312	-0.09	0.97
2328-5710	-0.13	1.06	2356-5511	-0.10	0.95
2329-5113	-0.19	1.19	2357-5611	-0.07	0.93
2329-5213	-0.12	1.05			

3 Method

Galaxy populations in the central regions of galaxy clusters are dominiated by old galaxies. (Demarco et al. 2005). This means that we are able to search for them in colour-magnitude space using a red sequence technique (Gladders & Yee 2000; Muzzin et al. 2009; Wilson et al. 2009). This chapter outlines how we applied the red sequence technique to a new dataset to find high-redshift galaxy cluster candidates. The stellar population models used to describe how we expect galaxies to evolve in time are also be discussed.

3.1 Galaxy stellar populations in galaxy clusters

Observations show that galaxy clusters are populated by galaxies that are older than non-cluster field galaxies (Demarco et al. 2005). Observations also show a subtle effect within the old population of galaxies: brighter and more massive galaxies in clusters have higher metallicities (Faber 1972; Loubser et al. 2009). A popular interpretation is the average metallicity of a galaxy increases as it becomes more massive. Metallicity describes the fraction of mass contained in a star that is heavier than hydrogen and helium. As the population of stars in a galaxy die in a supernova, they eject large amounts of metals into the intergalactic medium. If the host is a high mass galaxy, its gravitational potential well will hold on to these ejected metals, increasing its overall metallicity.

The brightest galaxy in a cluster, known at the brightest cluster galaxy (BCG), is expected to have a higher metallicity than the surrounding cluster members, and is reflected in the choice of models for this study. For the BCG we have assigned 60% solar and 40% twice solar metallicity and 100% solar metallicity for galaxies member galaxies which are ∼two magnitudes fainter than the BCG. From these two models we are able to mimic the slope of the red sequence, which is a colour-magnitude relation where old red galaxies are observed to follow a trend based on redshift.

3.1.1 Stellar population models

It is currently impossible to observe individual stars in distant galaxies as their angular size is much smaller than our present-day telescopes can resolve. What we are able to capture is the combination of all light sources in a galaxy, called its spectral energy distribution (SED). This distribution of light contains lots of information about the stellar population including stellar metallicity and star formation history (SFH).

The original stellar population models combined the spectra of many stars on different branches of the Hertzsprung-Russell diagram until they matched the galactic SED (Spinrad & Taylor 1971). By employing a quadratic programming approach to stellar population modelling, Faber (1972) was able to improve on the trial-and-error methods previously utilised. In the 1980s and 1990s, stellar evolution theory was used to limit the range of allowed stellar types, for a specified age and metallicity, used in stellar population synthesis models and has since become the standard modelling technique (Conroy 2013). These new models were able to accommodate for variations in ages, star formation history and even dust content.

Bruzual & Charlot (BC03; 2003) demonstrated that their popular stellar population models were able to repoduce the galaxy spectra in a data release from the Sloan digital sky survey (SDSS). They also have shown that the SFH and metallicity of these SDSS galaxies can be extracted by fitting observed spectra with their models. For these reasons, we use the BC03 model in the present work to model the galaxy cluster red sequence.

The SFH of galaxies on the red sequence of distant clusters is not very well constrained due to the scarcity of clusters known at these redshifts. Lidman et al. (2012) use a model with an exponentially declining SFH, starting at $z = 5$, to model the observer frame $J - Ks$ colour of BCGs from $z = 1.7$ to today. To match the colours, Lidman et al. (2012) use a model in which 60% of the stellar population has a solar metallicity and the other 40% has 2.5 times solar metallicity. The e-folding time scale of this model, $\tau = 0.9\,\mathrm{Gyr}$, is relatively large compared to other models that have been used to model the red sequence. While the model is a good fit to the $J - Ks$ colours of BCGs over this redshift range, it is not clear

that this model is appropriate for less luminous galaxies on the red sequence. There is an expectation from theoretical models (Tonini et al. 2012) that BCGs continue with low levels of star formation long after the star formation in other galaxies on the red sequence has ended, largely because low mass gas-rich galaxies merge with the BCG. For other galaxies in the cluster, such mergers are rarer.

Muzzin et al. (2013) use a model in which all the stars form at $z = 10$. This represents the other extreme. It is unlikely that all of the stars in galaxies on the red sequence are this old (Lidman et al. 2008) and coeval (Demarco et al. 2010). We therefore choose a model that is in between the one used in Lidman et al. (2012) and Muzzin et al. (2013). In our model, we form all of the stars at $z = 10$ with an e-folding time of $\tau = 0.3\,\mathrm{Gyr}$. Using this model, we simulate the older stellar population of a BCG using 60% solar metallicity and 40% twice solar metallicity. This model is also used with a 100% solar metallicity for member galaxies which are ∼two magnitudes fainter than the BCG.

The time evolving SED of our 100% solar metallicity model is shown in Figure 3.1 for the observer frame at different redshifts. The three band filters used in this this project are shown at the bottom of the plot. The transmission range for each filter is shaded in grey, and the peak transmission represented by the vertical dotted lines. This illustrates how the colours will evolve at different redshifts. The stellar bump feature (rest frame $1.6\,\mu$m) can clearly be seen to pass through the $3.6\,\mu$m and $4.5\,\mu$m filters at redshifts greater than 1. The $4000\,$Å break also passes through the z' band filter at higher redshifts. It is these features that will be used to determine the photometric redshift of galaxies observed in the $3.6\,\mu$m and $4.5\,\mu$m and z' bands.

3.2 Colours used in the Stellar Bump Sequence algorithm

Determining the redshift of an object with photometry relies on the fact that objects are brighter at some wavelengths than others. This strategy is most effective in wavelength regions (bands) when sharp features are present in the SED. This has traditionally been been exploited at $912\,$Å (Lyman break), $3800\,$Å (Balmer break) and the $4000\,$Å break. As mentioned previously, this work will focus on the $4000\,$Å break and the strong stellar bump feature at $1.6\,\mu$m as they redshift through the observer's z' ($9000\,$Å), $3.6\,\mu$m and $4.5,\mu$m bands. These features redshifting through the three bands used can be seen in Figure 3.1.

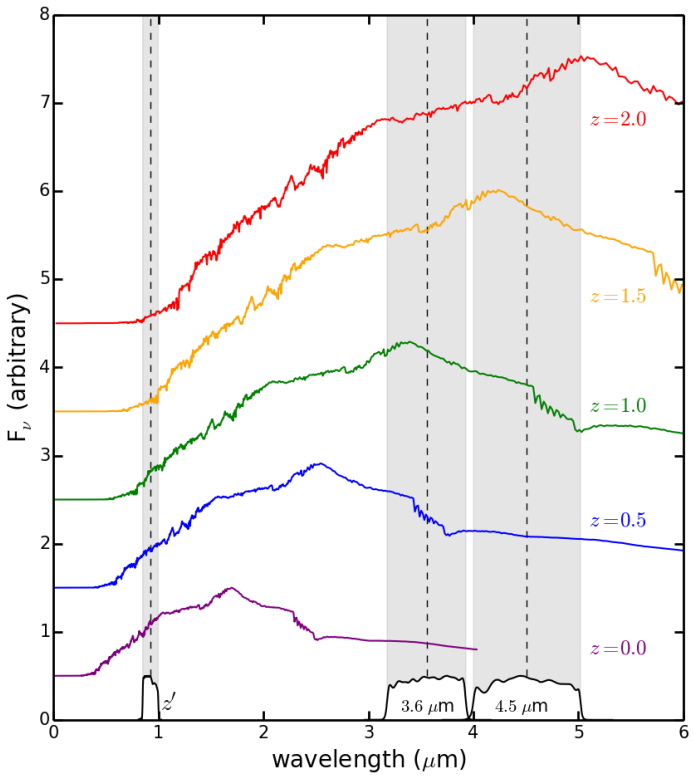

FIGURE 3.1: Time evolving SED through redhifts $z = 0.0$ to $z = 2.0$ from a 100% solar metallicity and $\tau = 0.3$ Gyr BC03 model. The three band filters used in this this work are overplotted at the bottom with the range of transmission shaded in grey and each peak illustrated with the vertical dotted line.

3.2.1 3.6 μm - 4.5 μm colour from IRAC data

The 1.6 μm stellar bump feature passes through the 3.6 μm and 4.5 μm bands with increasing redshift. Redshift $z \gtrsim 1$ galaxies have been observed to possess red 3.6 μm - 4.5 μm colours and negative k-correction values in the 3.6 μm and 4.5 μm bands (Papovich 2008). This was demonstrated by Papovich (2008) to be an effective way of determining the redshift of galaxies at $z > 1.3$.

The relation of 3.6 μm - 4.5 μm colour vs redshift is shown on the left side of Figure 3.2. If an object has a 3.6 μm - 4.5 μm colour < -0.1, it is impossible to precisely determine its redshift without additional information. This can be seen in the left panel of Figure 3.2 where colours < -0.1 do not uniquely map onto redshift. Figure 3.2 shows that 3.6 μm - 4.5 μm colours > 0.1 are also prone to projection effects due to redshift degeneracies. We are only able to assume a redshift of $z > 1.5$ for 3.6 μm - 4.5 μm colours redder than 0.1.

However, colours within the range of -0.1 to 0.1 behave linearly with redshift and are not degenerate. Therefore using the stellar bump feature alone for photometrically determining redshift is primarily useful in redshift ranges from $1.3 < z < 1.5$. This can also be used to make an initial colour cut to exclude all objects in a field that have a redshift of $z < 1.3$.

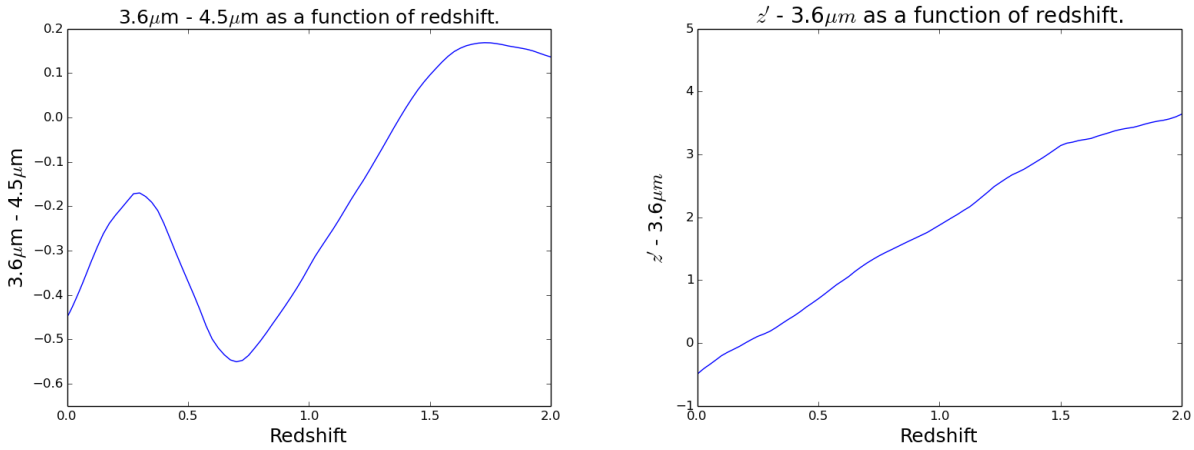

Figure 3.2: *Left:* 3.6 μm - 4.5 μm vs redshift. The use of this colour is contaminated by nearby objects at a redshift $z < 1.3$ as well as being prone to projection effects at $z > 1.5$. *Right:* z' - 3.6 μm vs redshift. This shows a monotonically reddening colour with increasing redshift. A colour cut can be made at z' - 3.6 μm < 1.75 to remove the nearby interlopers in the 3.6 μm - 4.5 μm model on the left. As the colour gets increasing red, deeper z' band observations are required for successful detections. Both sets of colours are determined using BC03 model with $\tau = 0.3$ Gyr and solar metallicity.

3.2.2 z' - 3.6 μm colour from DECam and IRAC data

As shown in Figure 3.1, the 4000 Å break passes through the z' band (9000 Å) at redshifts $z > 1$. The z' - 3.6 μm colour has successfully been used to find galaxy overdensities at a redshift of $z \approx 1.4$ in the SpARCS survey (Muzzin et al. 2009; Wilson et al. 2009). The z' - 3.6 μm colour evolution with redshift is shown in the right side of Figure 3.2. The z' - 3.6 μm colour shows a monotonically increasing value as redshift increases resulting in a unique mapping of colour to redshift. It should be noted that the colour becomes increasingly red at higher redshifts as galaxies in the z' band become very faint. The main problem with fainter z' band detections is that errors increase substantially, increasing the uncertainty of the photometric calculations. Therefore, extremely deep observations in the z' band are required in order to accurately estimate high redshifts.

Combining the two colours (z' - 3.6 μm and 3.6 μm - 4.5 μm) helps to overcome the shortcomings of using each separately. The z' - 3.6 μm colour is used to exclude interlopers

at $z < 0.85$ from 3.6 μm - 4.5 μm colours in addition to reducing any projection effects present at redshifts $z > 1.5$ in the 3.6 μm - 4.5 μm detections.

3.2.3 Variations in colour evolution with star formation history

The SFHs of red sequence high-redshift galaxies are poorly constrained. As a result, the corresponding colour evolution is currently unknown. This can be seen in Figure 3.3 where the colours from two different SFHs are plotted against redshift.

The choice of star formation history used to map colour onto redshift, especially in z' - 3.6 μm, has a large effect on redshift estimations. The z' - 3.6 μm colour evolution for two different SFHs have been plotted in the right side of Figure 3.3. Both models have 60% solar and 40% twice solar metallicities with $\tau = 0.3$ Gyr being represented by the solid blue line, and $\tau = 0.9$ Gyr being represented by the dashed green line. At redshifts of $z > 1.3$ the z' - 3.6 μm colours start to greatly differ as the $\tau = 0.9$ Gyr model stops increasing, similar to what is observed in the 3.6 μm - 4.5 μm colours at $z > 1.5$. As τ is a very uncertain parameter, the difference in models illustrates the uncertainty in redshift estimations from the z' - 3.6 μm colour beyond a redshift of $z > 1.0$. This difference between models has two important implications. Firstly, for $z > 1.0$, the red sequence may not be well defined in the z' - 3.6 μm colour. Secondly, redshifts estimated from the z' - 3.6 μm colour may be systematically wrong.

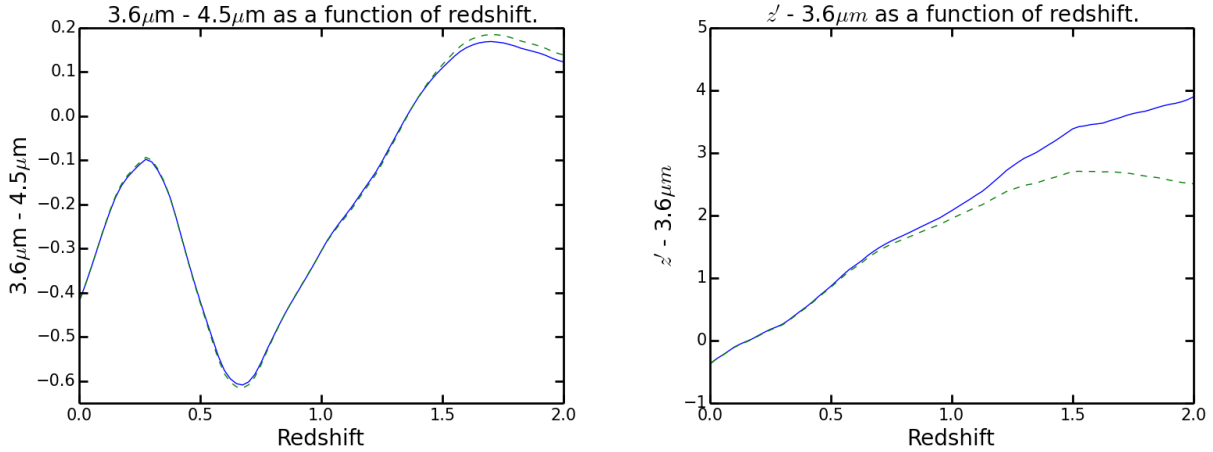

FIGURE 3.3: *Left:* 3.6 μm - 4.5 μm colour vs redshift for two different star formation histories: $\tau = 0.3$ Gyr for blue solid line and $\tau = 0.9$ Gyr for the green dashed line. At high redshifts ($z > 1.5$) the three models deviate slightly, but are within the uncertainties of the colours, which shows that these colours aren't sensitive to star formation histories. *Right:* z'-3.6 μm colour vs redshift for the same models. This clearly shows how sensitive the z'-3.6 μm colour is at high redshifts as using $\tau = 0.9$ Gyr results in projection effects at $z > 1.5$. For this study, the model represented with the blue solid line ($\tau = 0.3$ Gyr) was used.

The 3.6 μm - 4.5 μm colours are less affected by star formation history. The left side of Figure 3.3 demonstrates, for the two different star formation histories ($\tau = 0.3$ Gyr and $\tau = 0.9$ Gyr), that the colours deviate only slightly at redshifts of $z > 1.5$. This illustrates that the red sequence should be present at $z \sim 2$ and that the 3.6 μm - 4.5 μm colour can be used as an unbiased estimator of the redshift up to $z = 1.5$. Beyond $z = 1.5$, the 3.6 μm - 4.5 μm colour is no longer a powerful redshift estimator because the colour is flat with redshift.

3.2.4 Red sequence of early type cluster galaxies

Rich galaxy clusters have been observed to follow a strict colour-magnitude relation (Gladders & Yee 2000), known as the red sequence. Gladders & Yee (2000) demonstrated that even in contaminated fields, the red sequence can still clearly be seen. The red sequence forms a ridge in a colour-magnitude plot whose slope can be estimated by comparing the magnitudes of galactic populations with different metallicities. This feature is also sensitive to redshift making it a valuable tool in photometric redshift estimations. The red sequence can be used to estimate redshift based on photometric colours, which are much more easily obtained than spectra. Figure 3.4 shows how the red sequence varies with redshift using a BC03 model with $\tau = 0.3$ Gyr and a formation redshift of $z_f = 10$. We model the red sequence by computing the colours at two ends of the sequence. At one end is a model representing the BCG, which has a mixture of metallicities (60% solar and 40% twice solar) and at the other end is a model with 100% solar metallicity. The magnitude difference between these models is set so that we match the slope of the red sequence of the cluster RDCS 1252 at $z = 1.23$. The BCG model was used to calculate the colour-redshift relations used in the plots shown here for illustration purposes.

3.3 Modified red sequence method and the Stellar Bump Sequence algorithm

The methods presented here find clustered galaxies at particular redshifts photometrically, and require observations in the three bands discussed above. Source extracted catalogues of z' band DECam observations and 3.6 μm and 4.5 μm Spitzer observations in the XXL-S field were used, as discussed in Chapter 2.

This section will outline two methods we used to create our galaxy cluster candidate catalogues, a z' and 3.6 μm red sequence method and the SBS algorithm. The processes

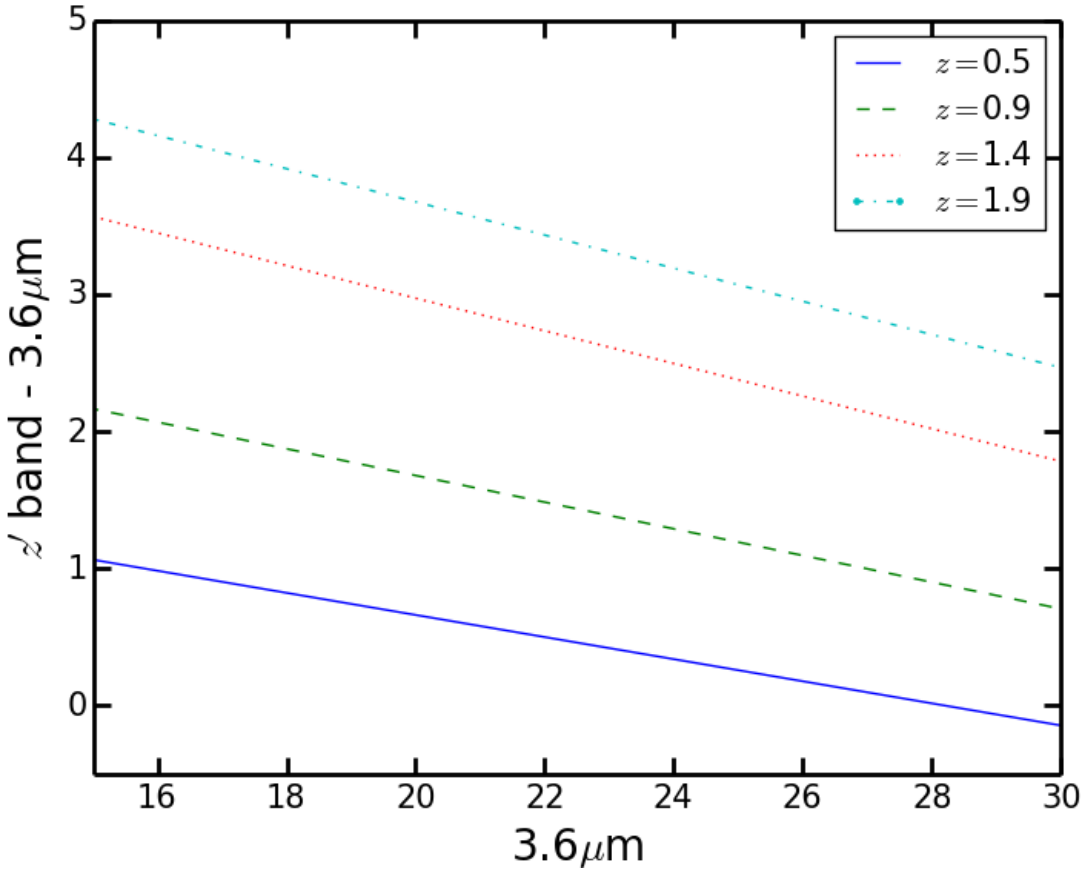

FIGURE 3.4: Colour-Magnitude diagram demonstrating how the red sequence behaves at different redshifts. This was calculated using two BC03 stellar models that have different metallicities to simulate the differences between the BCG and fainter cluster members. Colours were determined using the two models to find the slope of the red sequence at each redshift.

employed are outlined in Figure 3.5. These two methods run largely in parallel using the z' - 3.6 μm and 3.6 μm - 4.5 μm catalogues until generation of the final density maps. First, we estimate the redshift of each object based on its colour relative to the red sequence as a function of redshift. These objects are given a weight to indicate the likelihood of being at the designated redshift and will hereafter be referred to as colour weights. We then use these colour weights to determine the probability each object is part of a galaxy cluster based on spacial clustering and its magnitude compared to our model. Probabilities and colour weights from the z' - 3.6 μm catalogue are combined to create a final z' - 3.6 μm selected cluster density map. The z' - 3.6 μm output is then used to constrain the 3.6 μm - 4.5 μm detections, which yields higher quality 3.6 μm - 4.5 μm selected density maps. The two sets of density maps are then source extracted to create two cluster candidate catalogues.

3.3.1 Colour slice weight maps

The algorithm searches the colour-magnitude parameter space for red sequence signatures. The first step is similar for both colours, with the exception of a z' - 3.6 μm > 1.75 colour cut being made in the 3.6 μm - 4.5 μm catalogue to remove projection effects from objects at redshifts $z < 0.85$. This is demonstrated in the left plot of Figure 3.2.

The algorithm steps by $\delta z = 0.025$ from redshifts $z = 0.4$ to $z = 2.1$ using the z' - 3.6 μm colour and redshifts $z = 0.8$ to $z = 2.1$ for 3.6 μm - 4.5 μm. We chose δz to be much smaller than the uncertainty in the objects colour to ensure a high level of accuracy when assigning redshift. An object is labelled as good (i.e. a galaxy) if it is not flagged as a star by SExtractor (`CLASS_STAR` < 0.95) and its magnitude is above the sensitivity limit of the band observed (to remove spurious detections). We first create a colour slice by selecting galaxies with colours within 0.1 magnitude of the expected location of the red sequence at the current redshift being examined. The left side of Figure 3.6 is an example of one such colour cut. Here the red sequence is shown as a solid line with the limits shown in dashed lines. Objects with a colour uncertainty large enough to fall within the 0.1 magnitude limit of the red sequence, which might otherwise be omitted, are included in the cut.

All of the objects in the slice are then weighted according to their proximity to the red sequence and the size of their error. Objects have a higher weight if they possess a small error and are close to our theoretical red sequence. The weighting process is graphically represented in the right side of Figure 3.6. A Gaussian is generated for each object with a width equal to the error for each detection. This Gaussian is then integrated to calculate its area within the dispersion limit. All objects whose error is entirely within the dispersion will have the maximum weighting.

A raw weight map is then created with pixels that have been resampled from the original image to a 125 kpc size. As the resolution is much lower in the new pixel grid, the weights of all objects are binned onto the new scale as determined by their spatial location. This weight map is then spatially smoothed by convolving with a Gaussian kernel as illustrated in Figure 3.7. The resulting weight map shows regions that have a higher concentration of detections with high weight values, which are the first estimations of where galaxy cluster candidates are in the slice.

3.3.2 Determining cluster probability based on galaxy magnitude

The next two steps are the same for both colours. As uncertainties are present in the colour of each object, weight maps for each colour slice should be combined and not examined individually. The weight maps for each colour slice within a redshift of $z \pm 0.1$ are combined.

This cumulative weight map is then analysed to find density levels across the image. Each detection in the top 10% densest regions of the image is flagged as a potential cluster galaxy, with all other detections marked as field galaxies, as outlined by Muzzin et al. (2013). The probability (that a detection is a cluster galaxy) as a function of magnitude is then determined for the image. This is calculated by determining how the magnitude, M, of the flagged potential cluster galaxies compare to the fainter member galaxies theoretical magnitude, M^*, as calculated by our 100% solar metallicity model. Figure 3.8 shows this mapping of probabilities as a function of magnitude for one such colour slice with a linear fit being applied. From the linear fit it can be deduced that galaxies that are brighter than the faint theoretical model will be assigned a higher probability. Galaxies which are very bright ($M - M^* < -1.5$) have their probability determined by fixing their brightness to $M - M^* = -1.5$.

3.3.3 Final density maps

The weights found in the first step, and the magnitude probability relation in the second step, are combined to create a final density map for each redshift slice using both colour models, z' - 3.6 μm and 3.6 μm - 4.5 μm. This combination is accomplished by scaling the weights by their associated magnitude probabilities to increase the contrast between likely cluster galaxy candidates and field galaxies in the slice. The resulting weight map is then smoothed by convolution with a Gaussian kernel whose full width at half maximum corresponds to 0.5 Mpc. A pixel map is also created to flag all unsuitable pixels by setting those with a weighting of less than 0.001 to 0, and all other pixels to 1.0.

The final step of the algorithm combines the two bad pixel maps to remove projection effects that could be present in the 3.6 μm - 4.5 μm model at $z > 1.5$. This also improves the detection accuracy, as these cluster candidates are found using both colours. The final density map is then run through SExtractor to detect dense regions, which we label as cluster candidates at the redshift being investigated. The SExtractor settings used to identify overdense regions in the final clusters maps are shown in Table 3.1. We will discuss how well our algorithm detects galaxy clusters at redshifts $z < 1$ in Chapter 4 through comparison with other galaxy cluster catalogues. Future spectroscopic work is required to validate our galaxy cluster candidates at $z > 1$.

The SBS method is only effective for finding cluster candidates at redshifts $z > 0.85$ due to the colour cut made in the 3.6 μm - 4.5 μm. The z' - 3.6 μm data must be investigated independently to find cluster candidates at lower redshifts.

Table 3.1: SExtractor settings used for finding overdensities in the final cluster maps

Parameter	Setting
DETECT_MINAREA (pixel)	15
DETECT_THRESH(sigma)	5.0
FILTER	default.conv
DEBLEND_NTHRESH	32
DEBLEND_MINCONT	0.005
BACK_SIZE (pixel)	64
BACK_FILTERSIZE	3
BACKPHOTO_TYPE	GLOBAL

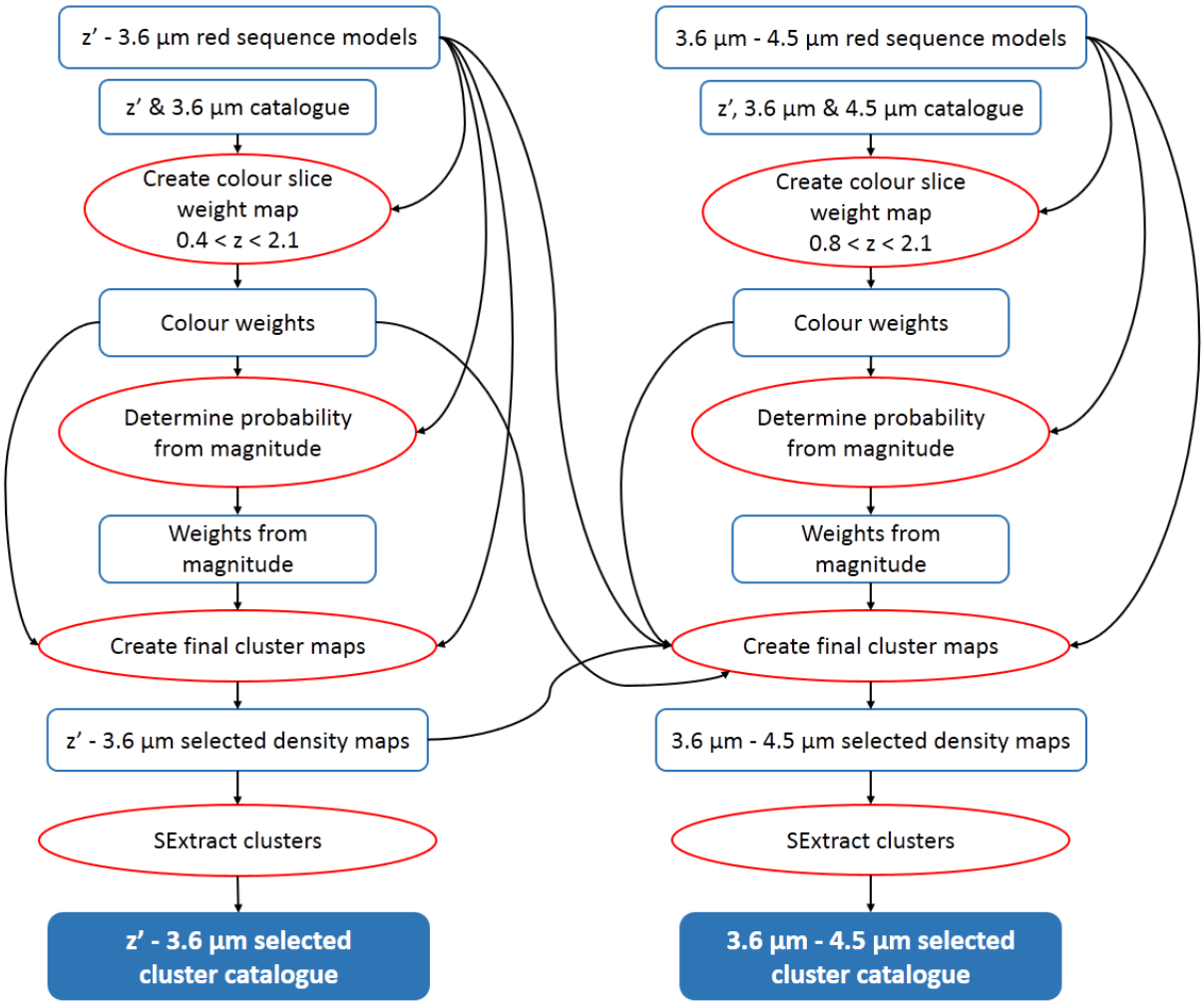

Figure 3.5: Flowchart outlining our cluster candidate finding process. Data is represented by blue boxes and processes in red ovals. The SBS algorithm runs largely in parallel until the creation of the 3.6 μm - 4.5 μm selected density maps. This algorithm creates two cluster candidate catalogues (solid blue boxes): a z' - 3.6 μm selected catalogue and a 3.6 μm - 4.5 μm selected catalogue.

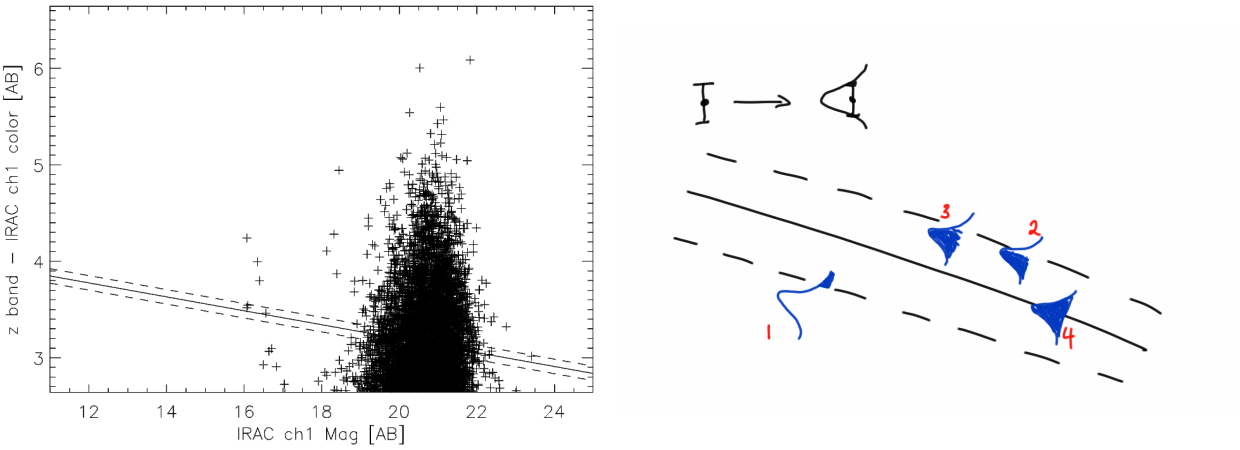

FIGURE 3.6: *Left:* z'-3.6 μm colour *vs* 3.6 μm of objects being analysed. The crosses are each object in the catalogue. The solid line represents the red sequence at the selected redshift and the dashed lines show the allowed limit around the red sequence that each object can have. A similar cut is made with the 3.6 μm - 4.5 μm colour. *Right:* Each detection that falls within the colour slice is given a weight. This weight represents the confidence that the object belongs to the slice. The error in colour of each detection is converted into a gaussian. The area under each gaussian that falls between the dispersion bounds is determined through integration and then normalised. Of the four detections shown, (1) has the lowest weighting, (2) the second lowest, (3) the third and (4) has the highest weighting. As can be seen, the two factors that influence a detections weight are the colour of the detection, as well as the size of the error. If the detections colour is within the slice and the error is very small, the weighting will be very high. All detections (and errors) that fall outside of the slice will have a zero weighting. Detections whose errors are containing entirely within the slice will have the highest weighting.

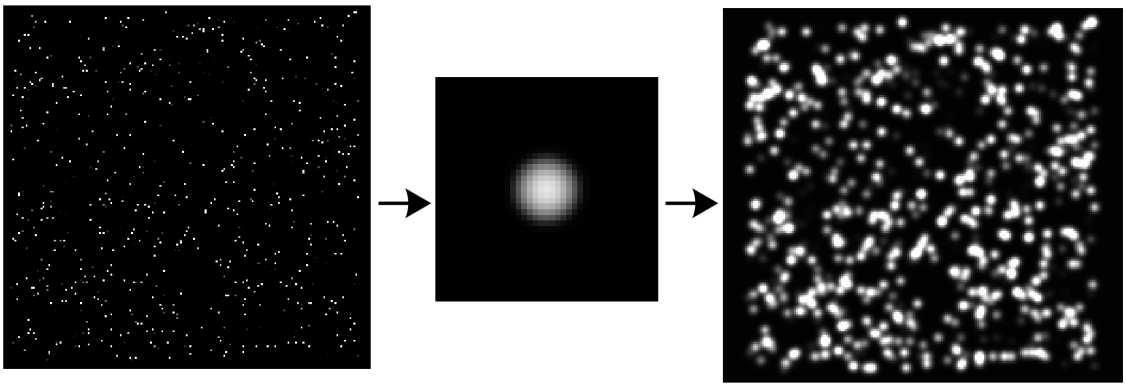

FIGURE 3.7: *Left:* The raw weights as determined by normalised Gaussian weighting for a colour slice. *Middle:* The raw weights are then convolved with a smoothing kernel. *Right:* The smoothed weight map. Regions in white have a high probability of containing galaxies in the colour slice and black areas have low probabilities.

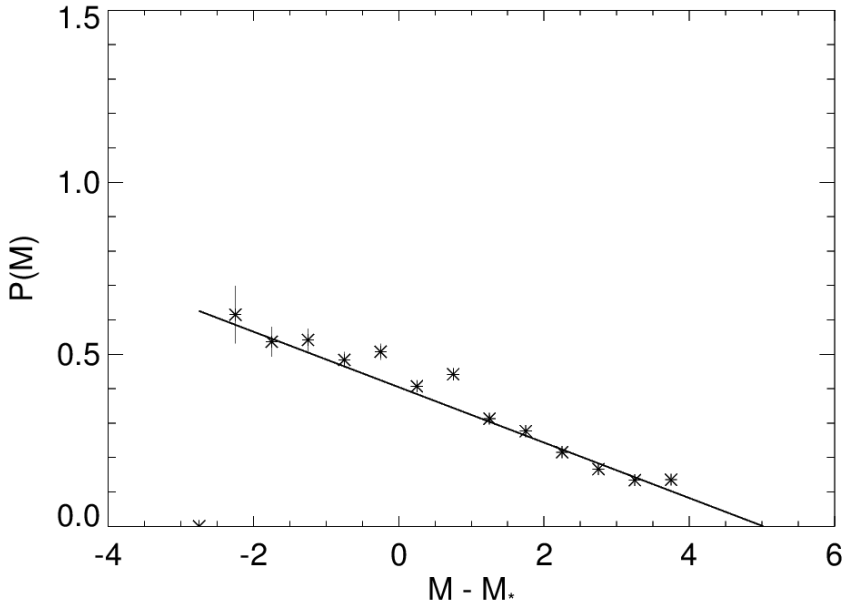

Figure 3.8: Probability magnitude plot showing the probability that the detected galaxies are cluster galaxies in the current colour slice based on their magnitudes compared to the model ($M - M_*$, measured and theoretical magnitudes respectively). A Linear fit is made to the points, with any zero probabilities being discarded.

4 Results

The candidate galaxy cluster catalogue was compiled using the SExtracted detections from the final density maps as discussed in Chapter 3. This chapter will outline the catalogue creation process, a brief analysis of the cluster candidates and end with a comparison to existing cluster catalogues in the XXL-S field.

4.1 Galaxy cluster candidate catalogue

The SExtractor catalogues derived from our density map slices are combined to create a single catalogue containing all of the galaxy cluster candidates detected. The redshift of each cluster candidate is estimated from the density map slice in which the cluster candidate of interest appears with the highest probability. This process is required due to uncertainties in redshift estimation when creating the colour slice weight maps. There are three sources of uncertainty in photometrically determining an objects redshift: flat 3.6 μm - 4.5 μm colour at $z > 1.5$, choice of star formation history in the z' - 3.6 μm colour and colour scatter around the red sequence. These uncertainties are located in redshift-space, which means a cluster candidate can appear in multiple density map slices. The SExtractor catalogues are iteratively examined prior to building the final catalogue to locate any duplicate detections within $z \pm 0.3$ of each other. If no duplicates are found, then the cluster candidate is added

directly to the final catalogue without any further analysis.

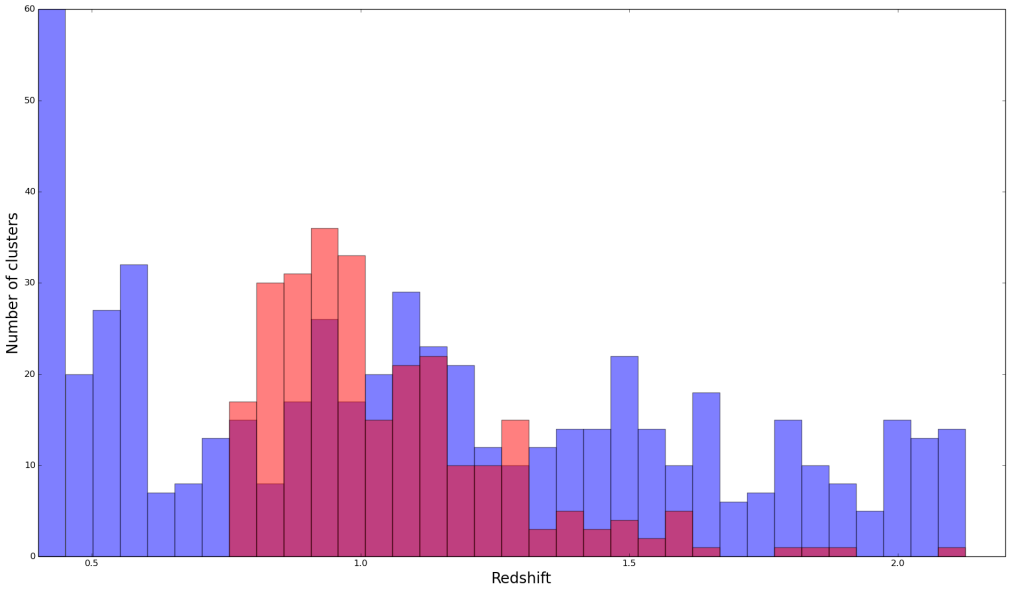

FIGURE 4.1: Histogram showing the redshift distribution of detected sources. The blue bars represent cluster candidates detected with the z' - 3.6 μm red sequence method and the red bars are for the SBS method. We attribute the spike in z' - 3.6 μm detections at $z = 0.4$ to interlopers at $0.35 < z < 0.4$. At high redshifts ($z > 1.3$), we accredit the amount of z' - 3.6 μm detections to random fluctuations in the galaxy distribution and, to a lesser extent, our z' band photometry being noisy at these faint magnitudes.

Our final galaxy cluster candidate catalogue contains 802 unique detections from redshifts $z = 0.4$ to $z = 2.125$. This is more than the 115 we predicted using the halo mass function outlined by Tinker et al. (2008), and indicates fine tuning of the algorithm may be required. The redshift distribution of our catalogue is shown in Figure 4.1 in which the blue bars represent the z' - 3.6 μm red sequence detected cluster candidates and the red bars indicate the Stellar Bump Sequence (SBS) detections.

We attribute the excess of cluster candidates at the lower limit of our redshift range, $z = 0.4$, to foreground cluster candidates in the range $0.35 < z < 0.4$. This effect was also seen at $z = 0.8$ for the SBS detected cluster candidates but is less prominent due to the redshift bin size. The large number of cluster candidates at $z > 1.3$ detected using the z' - 3.6 μm red sequence method can be attributed to random fluctuations in galaxy distribution and, to a lesser extent, noisy photometry as these are very faint objects in the z' band. The entire catalogue is listed in Appendix A.

The significance is calculated by determining the signal-to-noise ratio of all detections

in the density maps. The backgound (i.e. noise) in each density map is computed by measuring the flux from a randomly placed aperture, while simultaneously using a SExtractor generated segmentation map, which shows the locations of all detected sources, to ensure only background pixels are being counted. This process is repeated 1000 times, measuring the flux within each aperture with every iteration. Background noise is then estimated to be half the interval that contains the central 67% of the background flux counts. The flux for each source in the current density map is then divided by this background noise to give the significance value ξ, as listed in the final catalogue in Appendix A, and ranges from 5.8 to 35.

Of the 802 candidates, there are 225 at redshifts $z \geq 1.3$. 199 of these were detected using the z' - 3.6 μm red sequence method, 35 using the SBS method and of these, nine were found using both methods. False colour images of these nine are shown in Figure 4.2 with green circles representing the candidate cluster members and the red circle is 2', $\sim$1 Mpc at $z = 1.0$, in diameter centred on the cluster candidate detection. The colour in these images was created using z' band as blue, 3.6 μm as green and 4.5 μm as red. The galaxies highlighted in these images were selected by including only those that possess a weight greater than 0.5, as found in the colour slice weight maps. The clustering of galaxies is especially obvious in the bottom middle image.

Figure 4.3 contains images of six cluster candidates we detected which are also in the X-ray selected catalogue. The bottom right image is the only cluster candidate in Figure 4.3 without spectroscopic confirmation, but has the highest redshift of all matches in the catalogue at $z = 1.075$. The red circle is a 2', $\sim$1 Mpc at $z = 1.0$, in diameter centred on the cluster candidate detection and the green circles mark candidate cluster members with a weighting greater than 0.5.

Figure 4.4 contains six new cluster candidates detected using the $z' - 3.6\mu$m red sequence method and are located at a redshift of $z \sim 0.5$. Candidate cluster galaxies with a weighting greater than 0.5 are circled in green, and the center of the detection is marked by a 2', $\sim$750 kpc at $z = 0.5$, diameter red circle.

Figure 4.5 shows three density maps of the XXL-S field at redshifts $z = 0.5, 1.0$ and 1.5. The red circles show detections in our catalogues, blue circles are detections in the X-ray catalogue from Pierre et al. (in preparation) and the green circle is a millimetre selected cluster from Bleem et al. (2014b). These detections are discussed further in Section 4.2 below. Cluster detections are only shown here if their redshift is $z \pm 0.05$ of the density slice. These three density maps were generated using the z' - 3.6 μm red sequence method.

4.2 Comparison with other work

Over the last decade optical, X-ray and millimetre surveys (Desai et al. 2012; Pierre et al. 2011; Ashby et al. 2013; Chang et al. 2009) have been used to search for galaxy clusters in this region of sky. We compare our catalogue with four galaxy cluster studies that overlap the XXL-S field; two optical (Bleem et al. 2014a; Rettura et al. 2014), a millimetre (Bleem et al. 2014b) and an X-ray (Pierre et al., in preparation). We have cross-matched these catalogues with our own and have marked any matches in Appendix A. We consider a match to be any cluster candidate within 1 Mpc and $z \pm 0.1$ for spectroscopically confirmed, or $z \pm 0.2$ for photometrically determined redshift.

Pierre et al.'s (in preparation) x-ray selected catalogue contains 101 $z > 0.3$ clusters in the XXL-S field with 67 of these being spectroscopically confirmed. The location of some of these clusters can be seen as blue circles in Figure 4.5. Using the z' - 3.6 μm red sequence method we were able to detect 41 of the catalogued x-ray clusters, 32 of which are spectroscopically confirmed, eight at photomeric and one that has a tentative redshift.

Bleem et al.'s 2014b Sunyaev-Zel'dovich effect selected cluster catalogue contains ~ 17 clusters in the XXL-S field with a redshift of $z > 0.3$. One of these clusters is represented by a green circle in Figure 4.5. We find that there are five matches in our catalogue, all of which were found with the z' - 3.6 μm red sequence method.

One optically selected catalogue was from the SSDF survey. At the time of writing, Rettura et al. (2014) have only made their 10 most significant detections with $z > 1.3$ available, six of which are in XXL-S. We found two of these six cluster candidates in our catalogue. The second optically selected catalogue is from Bleem et al. (2014a), with ~ 290 clusters in XXL-S with $z > 0.3$. We found 60 of these cluster candidates in our catalogue with five having a redshift $z > 0.8$, three of which were found using the SBS method.

Using the z' - 3.6 μm red sequence method and the SBS method we found 802 galaxy cluster candidates in the XXL-S field. Cross-correlating our catalogue with those available in the literature we found 81 corresponding cluster candidates. This confirms our two methods are successful in photometrically selecting galaxy clusters at redshifts $z > 0.4$. In total, we present 721 new cluster candidates in the XXL-S field.

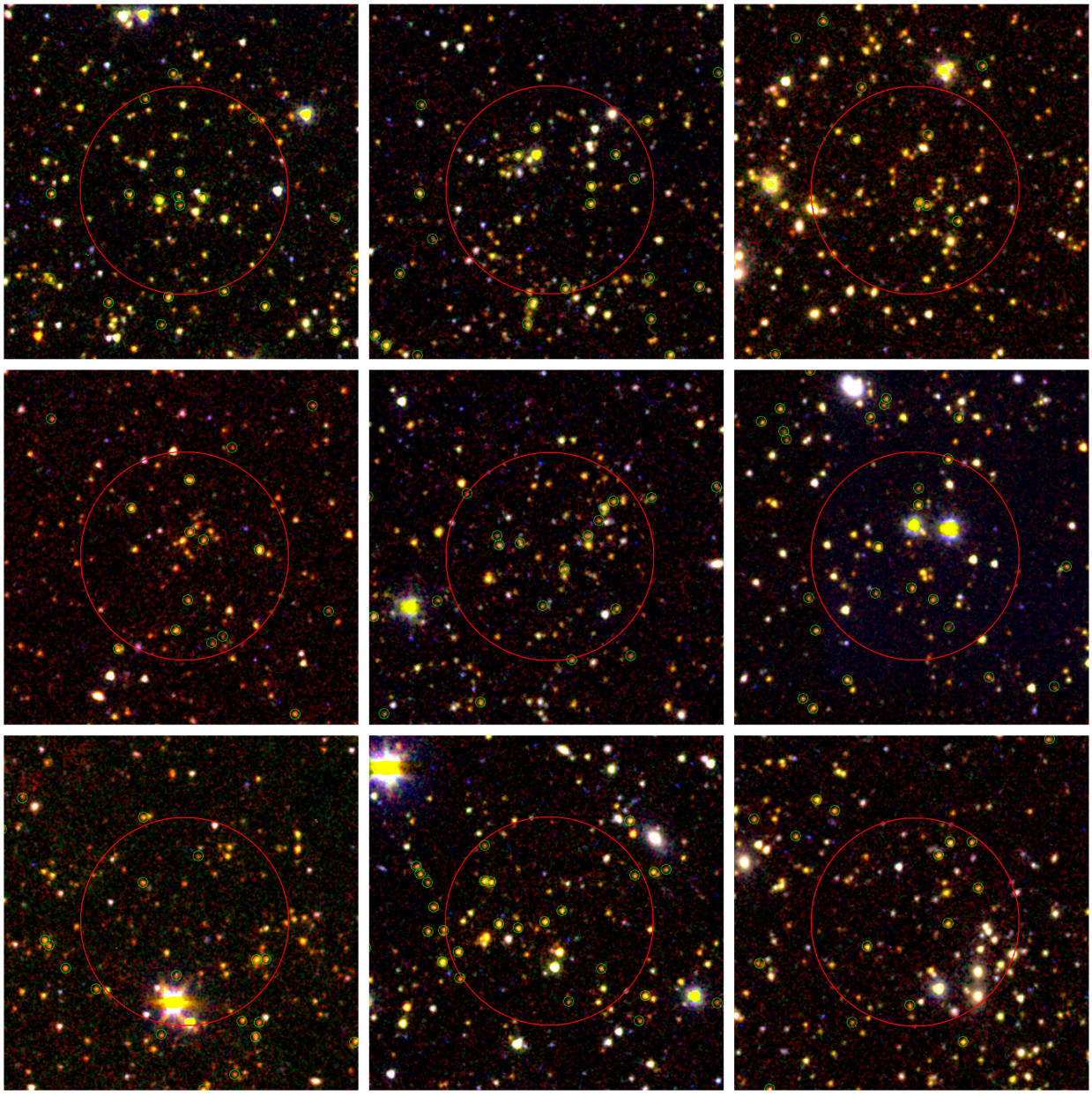

Figure 4.2: False colour images of the nine galaxy cluster candidates found by both methods, z' - 3.6 μm red sequence and SBS, at $z > 1.3$. North is up, and east is to the left. These cluster candidates have a redshift of (*top row, left to right*): 1.3, 1.3, 1.325 (*centre row, left to right*): 1.325, 1.375, 1.475 (*bottom row, left to right*): 1.525, 1.65, 1.825. The red circles represent $\sim$1 Mpc at $z = 1.0$ (2') centred on the cluster candidate detection and the green circles mark galaxies which are located at each corresponding redshift.

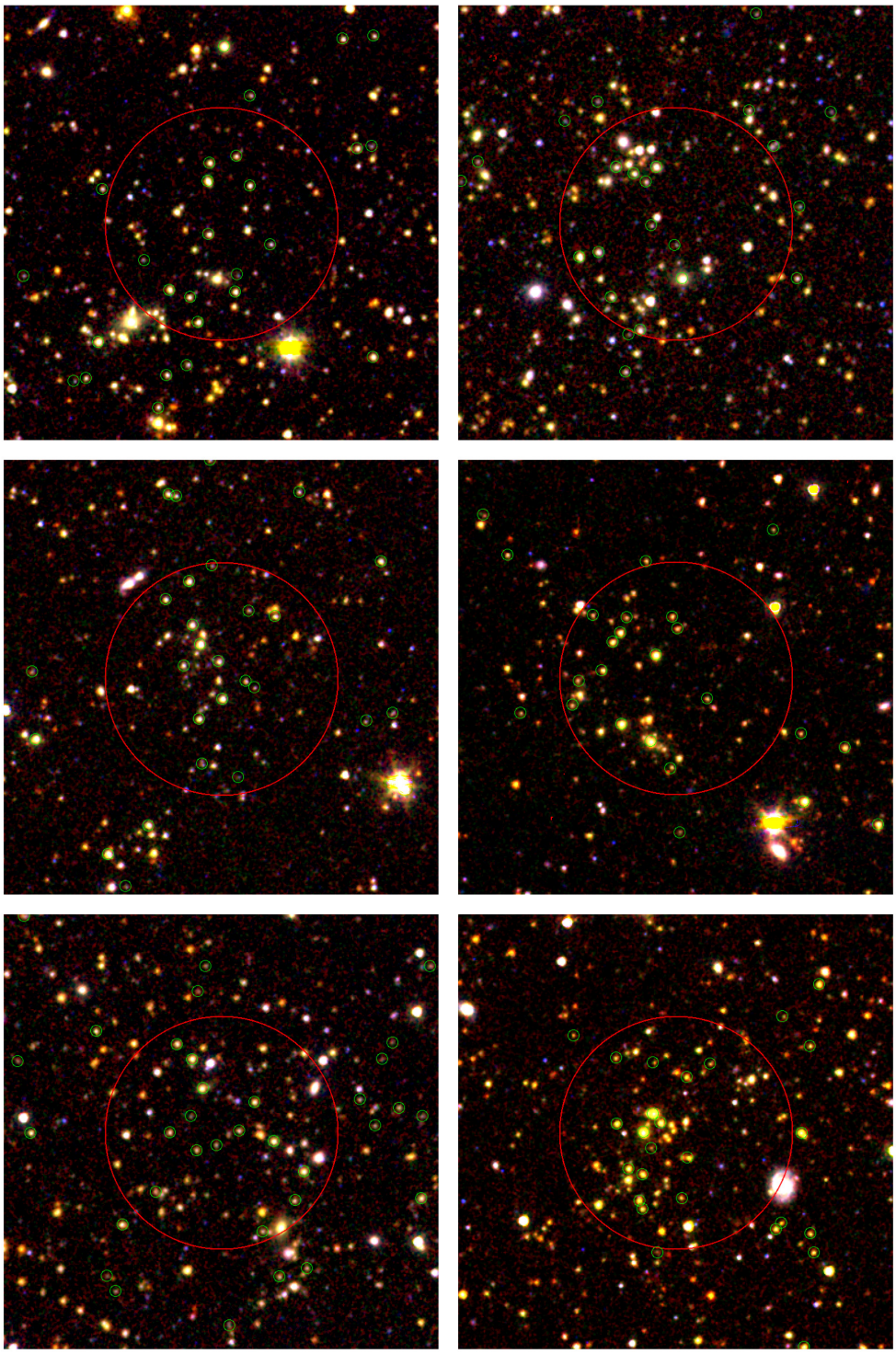

FIGURE 4.3: False colour images of six galaxy cluster candidates matches with the X-ray selected catalogue. North is up, and east is to the left. All cluster candidates shown have been spectroscopically confirmed except for the bottom right image, which has the highest redshift of our matches at $z = 1.075$. These cluster candidates have a redshift of (*top row, left to right*): 0.575, 0.65 (*centre row, left to right*): 0.675, 0.775 (*bottom row, left to right*): 0.825, 1.075. The red circles represent $\sim$1 Mpc at $z = 1.0$ (2') centred on the cluster candidate detection and the green circles mark galaxies which are located at each corresponding redshift.

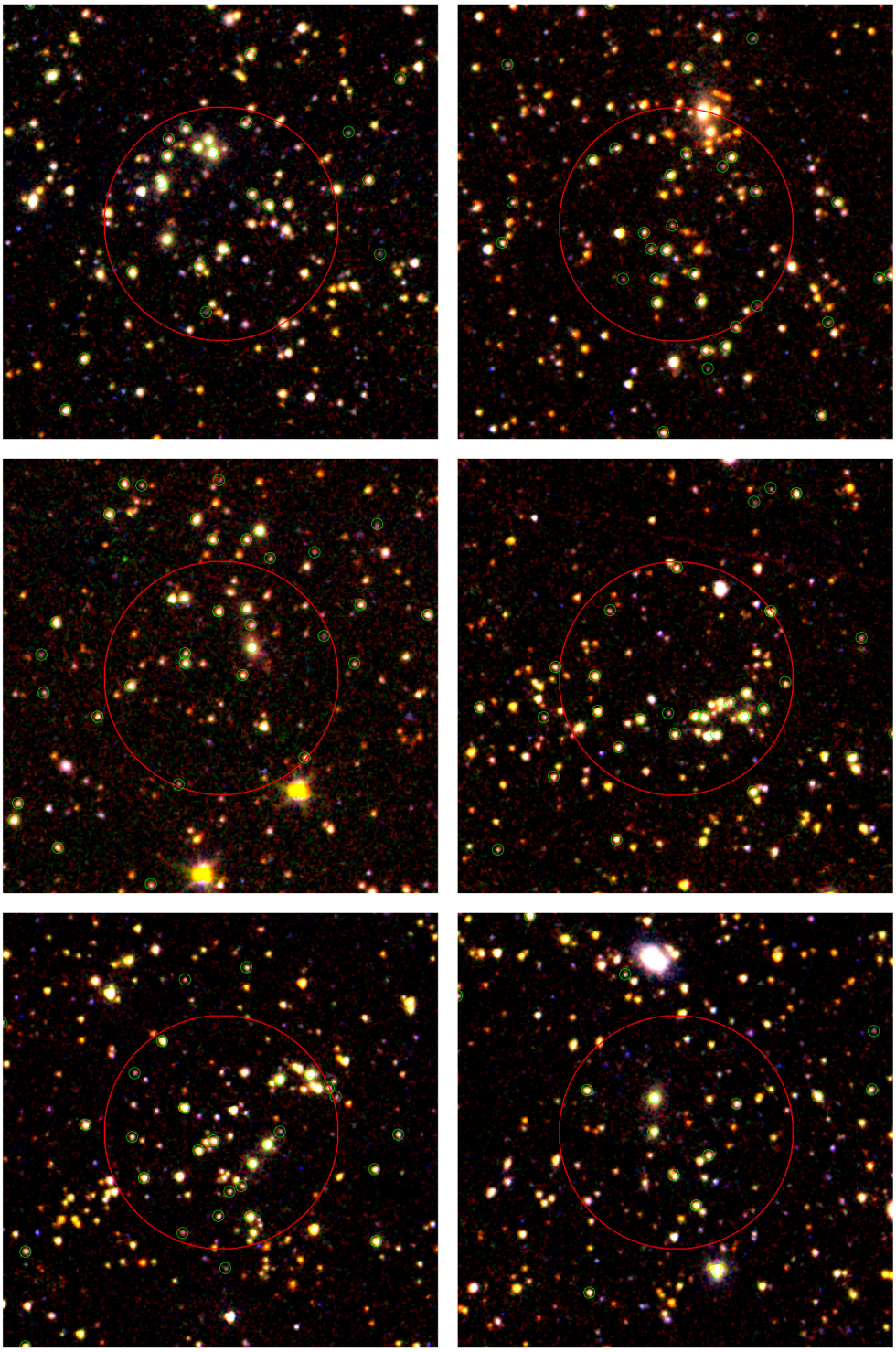

Figure 4.4: False colour images of six galaxy cluster candidates found at a redshift of $z \sim 0.5$. North is up, and east is to the left. The redshift of each cluster candidate pictured is (*top row, left to right*): 0.45, 0.475 (*centre row, left to right*): 0.5, 0.525 (*bottom row, left to right*): 0.55, 0.55. The red circles represent $\sim$750 kpc at $z = 0.5$ (2') centred on the cluster candidate detection and the green circles mark galaxies which are located at each corresponding redshift.

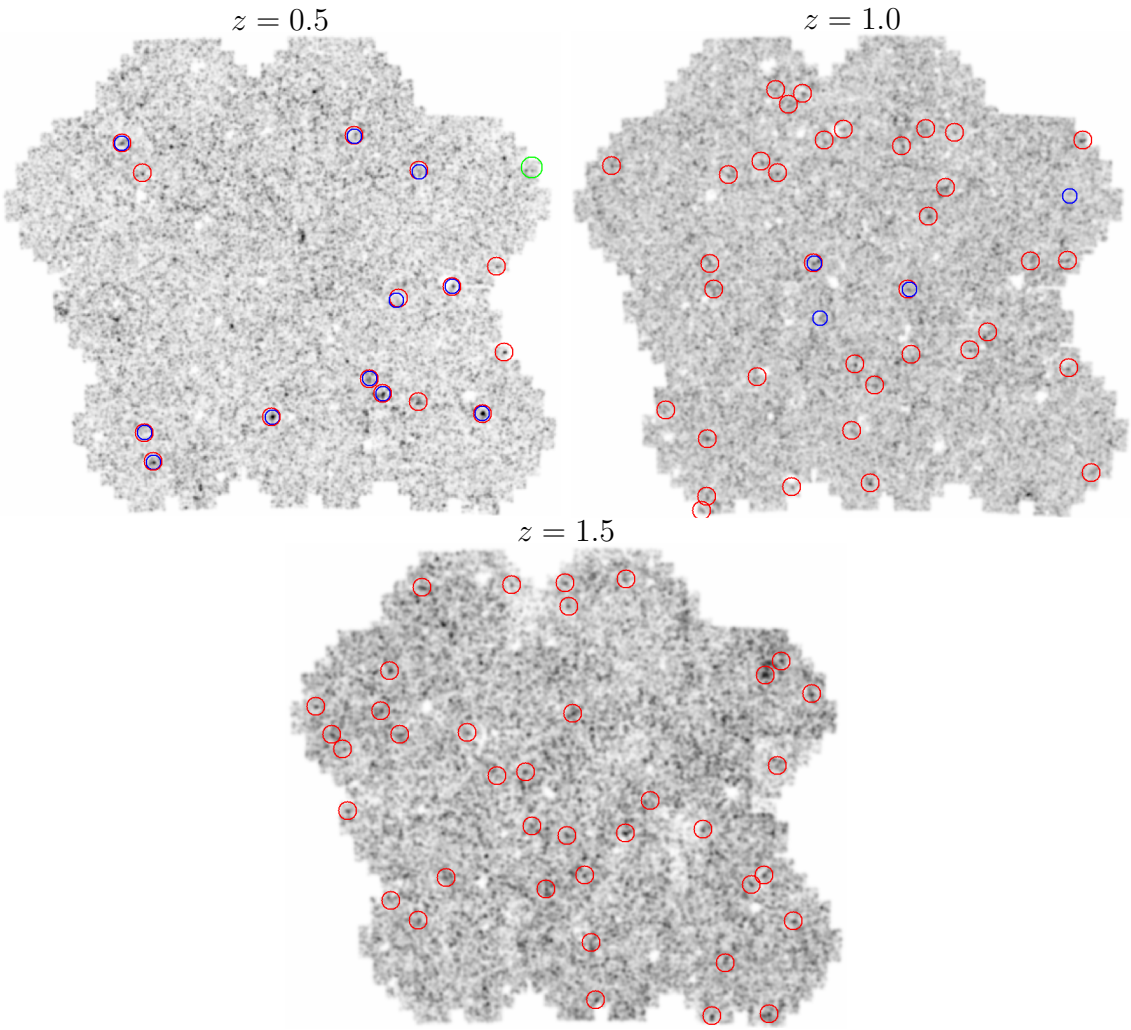

FIGURE 4.5: Density maps of the XXL-S field at three redshifts, $z = 0.5, 1.0$ and 1.5. Each circle represents a cluster candidate detection. Candidate clusters found in this work are circled in red, x-ray detected clusters (Pierre et al., in preparation) are shown in blue and a cluster found using the SunyaevZel'dovich effect (Bleem et al. 2014b) is marked with a green circle.

5

Conclusion and Future Studies

Our high redshift galaxy cluster candidate catalogue presents detections to a redshift of $z = 2.125$ and contains 802 cluster candidates, 721 of which were previously undetected. Two procedures were used to make detections: a z' and 3.6 μm red sequence method and the SBS method. Both of these red sequence based methods utilised object catalogues created from new DECam data in the z' band that was combined with existing Spitzer 3.6 μm and 4.5 μm IRAC catalogues.

The z' and 3.6 μm red sequence method uses z' DECam observations performed in July and August of 2013, combined with existing 3.6 μm Spitzer observations to find 595 cluster candidates at redshifts $0.4 < z < 2.125$. Of these 595 detections, 41 were catalogued X-ray detected cluster candidates, 32 of which have been spectroscopically confirmed. There were also five SZ selected clusters detected using this method.

The SBS method found 256 cluster candidates at redshifts $0.8 < z < 2.125$ using two colours created from z' band, 3.6 μm and 4.5 μm data. As most available catalogues are in the low-redshift environment, this method found less cluster candidates than previously detected. There were, however, three optically detected cluster candidates from the BCS at $z > 0.8$ that were detected using the SBS and not detected with the z' and 3.6 μm red sequence method.

We created an aperture corrected catalogue using SExtracted DECam z' band data, that

was cross-correlated with existing aperture corrected SSDF catalogues to create a final source catalogue that contains 2,137,515 unique objects in the XXL-S field. By aperture correcting our z' band detected sources, we were able to ensure high signal-to-noise photometry, which is essential for creating accurate galaxy colours.

Custom BC03 stellar population models were used in both detection methods to simulate the galactic red sequence, which were calibrated to match the red sequence observed in the cluster RDCS 1252 at $z = 1.23$. Each object in the catalogue was then redshift weighted based on both its scatter about the red sequence, and its brightness in comparison to our BC03 models. These weighted objects were then spatially binned and convolved with a Gaussian kernel that enabled the efficient detection of galaxy overdensities, which were subsequently flagged as galaxy cluster candidates.

The z' band and 3.6 μm data were used to make a z' - 3.6 μm > 1.7 colour cut that removed low-redshift ($z < 0.85$) interlopers from the SBS source catalogues. This z' - 3.6 μm colour also enabled the constraint of SBS determined redshifts of $z > 1.5$ as the 3.6 μm - 4.5 μm colour becomes degenerate at high redshifts.

We detect 802 galaxy cluster candidates, which is seven times greater than the predicted 115, suggesting we may have a large number of false positives. Therefore, the next stage in our analysis will be to fine tune our algorithm, to maximise both the purity of the sample and the efficiency of detection. Sample purity will ensure that all detections are galaxy clusters and detection efficiency will enable us to comprehensively detect all possible galaxy clusters.

Follow-up future research will be to use 8 metre class telescopes to spectroscopically confirm the most significant galaxy cluster candidates presented in the final catalogue. Once a cluster is confirmed, out to a potential redshift of $z > 2$, it will then be possible to conduct a detailed multi-wavelength study of its member galaxies with the aim to further our understanding of galactic evolution.

A

The cluster candidate catalogue

Table A.1: All cluster candidates found using both detection methods. The z' - 3.6 μm red sequence method we have labelled RS and the stellar bumb sequence method as SBS. The significance of the cluster candidate detection (ξ) is a signal-to-noise calculation for each cluster in each density map. Cluster candidates detected that are also found in the literature are listed in the *other* column

Cluster ID	R.A. (deg., J2000)	Dec (deg., J2000)	Redshift	ξ	RS	SBS	Other
DECam_J2311.4-5402	347.854	-54.0316	1.125	11.40	✓	✓	
DECam_J2311.2-5344	347.796	-53.7394	0.950	11.64	✓	✓	
DECam_J2310.4-5320	347.605	-53.3411	1.525	8.95	✓	✓	
DECam_J2310.4-5260	347.589	-52.9976	1.100	13.33	✓	✓	
DECam_J2317.5-5643	349.370	-56.7170	1.150	14.56	✓	✓	
DECam_J2318.2-5522	349.558	-55.3644	0.925	12.63	✓	✓	
DECam_J2315.7-5252	348.927	-52.8730	1.125	12.46	✓	✓	
DECam_J2313.2-5233	348.309	-52.5524	0.775	10.17	✓	✓	
DECam_J2318.3-5218	349.572	-52.3020	1.200	10.82	✓	✓	
DECam_J2323.4-5445	350.855	-54.7447	1.175	13.77	✓	✓	
DECam_J2324.6-5643	351.155	-56.7132	1.125	15.33	✓	✓	
DECam_J2324.8-5211	351.201	-52.1876	0.975	12.46	✓	✓	
DECam_J2321.7-5241	350.434	-52.6843	1.050	9.94	✓	✓	
DECam_J2319.1-5306	349.779	-53.0955	1.150	10.51	✓	✓	

Table A.1 —*Continued*

Cluster ID	R.A. (deg., J2000)	Dec (deg., J2000)	Redshift	ξ	RS	SBS	Other
DECam_J2328.7-5337	352.179	-53.6116	1.325	9.85	✓	✓	
DECam_J2328.6-5248	352.146	-52.8023	0.975	15.58	✓	✓	
DECam_J2327.3-5348	351.824	-53.7950	1.150	10.93	✓	✓	
DECam_J2328.8-5533	352.194	-55.5533	0.825	16.67	✓	✓	1
DECam_J2332.2-5514	353.049	-55.2254	1.650	11.25	✓	✓	
DECam_J2332.3-5655	353.079	-56.9094	0.975	18.90	✓	✓	
DECam_J2330.6-5640	352.656	-56.6719	0.950	11.13	✓	✓	
DECam_J2330.1-5240	352.522	-52.6691	1.025	10.28	✓	✓	
DECam_J2329.5-5223	352.384	-52.3886	1.300	10.19	✓	✓	
DECam_J2331.9-5239	352.964	-52.6579	1.825	7.64	✓	✓	
DECam_J2335.5-5322	353.883	-53.3749	0.800	10.90	✓	✓	
DECam_J2334.1-5308	353.515	-53.1365	1.225	10.71	✓	✓	
DECam_J2337.0-5343	354.239	-53.7103	1.025	14.39	✓	✓	
DECam_J2339.1-5531	354.773	-55.5108	1.300	10.28	✓	✓	4
DECam_J2337.2-5558	354.299	-55.9702	1.150	11.12	✓	✓	
DECam_J2339.8-5209	354.960	-52.1538	1.250	11.08	✓	✓	
DECam_J2339.8-5321	354.962	-53.3553	1.125	10.30	✓	✓	
DECam_J2344.6-5306	356.156	-53.1047	1.250	12.04	✓	✓	
DECam_J2340.3-5245	355.066	-52.7522	1.475	10.09	✓	✓	
DECam_J2342.7-5411	355.681	-54.1791	1.075	13.84	✓	✓	3
DECam_J2345.4-5437	356.344	-54.6102	1.175	10.29	✓	✓	
DECam_J2341.0-5404	355.245	-54.0623	1.375	12.64	✓	✓	4
DECam_J2340.7-5518	355.172	-55.2953	0.975	10.32	✓	✓	1
DECam_J2341.4-5535	355.340	-55.5872	1.000	13.28	✓	✓	
DECam_J2343.2-5622	355.792	-56.3685	1.325	15.04	✓	✓	
DECam_J2343.9-5543	355.983	-55.7153	0.900	15.54	✓	✓	
DECam_J2341.8-5633	355.453	-56.5524	0.925	11.59	✓	✓	
DECam_J2349.1-5243	357.274	-52.7201	0.975	24.37	✓	✓	
DECam_J2348.4-5333	357.105	-53.5445	0.850	17.08	✓	✓	
DECam_J2351.0-5334	357.746	-53.5674	0.950	11.82	✓	✓	
DECam_J2345.5-5253	356.367	-52.8845	0.950	19.50	✓	✓	
DECam_J2348.4-5410	357.108	-54.1659	1.000	9.66	✓	✓	
DECam_J2352.3-5559	358.076	-55.9864	1.150	10.48	✓	✓	
DECam_J2352.2-5633	358.051	-56.5545	1.075	14.35	✓	✓	
DECam_J2346.9-5702	356.719	-57.0293	0.825	13.77	✓	✓	
DECam_J2311.9-5340	347.972	-53.6641	0.900	10.19	✗	✓	
DECam_J2310.0-5319	347.511	-53.3147	0.975	9.19	✗	✓	
DECam_J2312.2-5310	348.057	-53.1640	0.975	11.70	✗	✓	
DECam_J2310.4-5333	347.607	-53.5488	1.125	7.59	✗	✓	
DECam_J2314.8-5642	348.694	-56.7061	0.800	10.99	✗	✓	

Table A.1 —*Continued*

Cluster ID	R.A. (deg., J2000)	Dec (deg., J2000)	Redshift	ξ	RS	SBS	Other
DECam_J2316.7-5657	349.183	-56.9525	0.925	9.19	✗	✓	
DECam_J2317.4-5711	349.348	-57.1905	0.975	9.04	✗	✓	
DECam_J2317.5-5654	349.386	-56.9026	1.625	8.00	✗	✓	
DECam_J2312.0-5451	347.995	-54.8450	0.800	9.86	✗	✓	
DECam_J2313.4-5451	348.346	-54.8580	0.825	9.88	✗	✓	
DECam_J2316.7-5449	349.171	-54.8128	1.300	14.70	✗	✓	
DECam_J2316.2-5526	349.049	-55.4274	1.325	10.14	✗	✓	
DECam_J2315.0-5628	348.762	-56.4639	0.825	9.68	✗	✓	
DECam_J2317.1-5640	349.266	-56.6671	0.900	9.44	✗	✓	
DECam_J2316.3-5622	349.077	-56.3605	0.900	10.36	✗	✓	
DECam_J2314.8-5558	348.688	-55.9688	1.050	9.10	✗	✓	
DECam_J2316.9-5554	349.232	-55.8936	1.200	9.16	✗	✓	
DECam_J2315.2-5628	348.791	-56.4664	1.225	9.86	✗	✓	
DECam_J2313.5-5249	348.380	-52.8163	0.800	10.53	✗	✓	2
DECam_J2317.0-5342	349.247	-53.6959	0.825	9.64	✗	✓	
DECam_J2315.7-5322	348.919	-53.3709	0.825	13.13	✗	✓	
DECam_J2317.5-5330	349.367	-53.5012	0.825	11.73	✗	✓	
DECam_J2313.4-5324	348.362	-53.3930	0.975	8.84	✗	✓	
DECam_J2318.3-5248	349.567	-52.8063	1.125	9.95	✗	✓	
DECam_J2316.6-5314	349.162	-53.2279	1.125	10.64	✗	✓	
DECam_J2315.0-5326	348.759	-53.4307	1.200	9.11	✗	✓	
DECam_J2316.4-5336	349.108	-53.6047	1.425	8.90	✗	✓	
DECam_J2312.4-5336	348.110	-53.5954	1.475	8.85	✗	✓	
DECam_J2314.3-5248	348.569	-52.8082	1.825	7.68	✗	✓	
DECam_J2312.8-5321	348.194	-53.3514	1.900	8.73	✗	✓	
DECam_J2315.5-5416	348.885	-54.2626	0.850	9.32	✗	✓	
DECam_J2313.0-5430	348.241	-54.4979	0.900	12.87	✗	✓	
DECam_J2315.8-5401	348.954	-54.0207	0.900	9.19	✗	✓	
DECam_J2317.2-5428	349.292	-54.4689	0.900	9.86	✗	✓	
DECam_J2315.6-5348	348.905	-53.7951	0.925	11.79	✗	✓	
DECam_J2313.0-5401	348.258	-54.0221	1.125	8.59	✗	✓	
DECam_J2313.9-5421	348.486	-54.3534	1.125	9.60	✗	✓	
DECam_J2317.3-5355	349.317	-53.9188	1.275	10.67	✗	✓	
DECam_J2315.8-5441	348.957	-54.6892	1.550	9.10	✗	✓	
DECam_J2314.6-5405	348.649	-54.0782	2.125	7.21	✗	✓	
DECam_J2316.8-5240	349.203	-52.6669	0.950	9.92	✗	✓	
DECam_J2319.3-5231	349.836	-52.5170	1.100	9.86	✗	✓	
DECam_J2318.9-5507	349.714	-55.1101	0.825	9.83	✗	✓	
DECam_J2325.2-5516	351.291	-55.2701	0.900	11.90	✗	✓	
DECam_J2323.6-5514	350.888	-55.2300	0.925	9.33	✗	✓	

Table A.1 —*Continued*

Cluster ID	R.A. (deg., J2000)	Dec (deg., J2000)	Redshift	ξ	RS	SBS	Other
DECam_J2319.8-5517	349.938	-55.2864	0.975	10.12	✗	✓	
DECam_J2319.3-5540	349.835	-55.6739	1.050	8.71	✗	✓	
DECam_J2322.1-5452	350.522	-54.8618	1.200	11.51	✗	✓	
DECam_J2320.1-5635	350.032	-56.5780	0.825	12.12	✗	✓	
DECam_J2321.9-5623	350.473	-56.3894	0.825	13.80	✗	✓	
DECam_J2319.4-5556	349.838	-55.9328	0.850	9.87	✗	✓	
DECam_J2323.3-5608	350.822	-56.1281	0.925	11.04	✗	✓	
DECam_J2319.5-5602	349.879	-56.0278	1.075	10.63	✗	✓	
DECam_J2318.7-5624	349.671	-56.3950	1.300	10.24	✗	✓	
DECam_J2318.4-5712	349.590	-57.1974	0.900	13.91	✗	✓	
DECam_J2323.3-5656	350.825	-56.9335	1.300	10.60	✗	✓	
DECam_J2323.2-5143	350.793	-51.7146	0.825	12.93	✗	✓	2
DECam_J2320.7-5204	350.183	-52.0656	0.900	10.65	✗	✓	2
DECam_J2319.5-5201	349.874	-52.0089	1.150	9.41	✗	✓	
DECam_J2323.1-5221	350.783	-52.3526	1.175	9.20	✗	✓	
DECam_J2320.8-5225	350.204	-52.4084	1.275	13.76	✗	✓	
DECam_J2324.9-5329	351.230	-53.4776	0.825	11.48	✗	✓	
DECam_J2320.9-5311	350.223	-53.1847	0.975	9.92	✗	✓	
DECam_J2321.9-5245	350.480	-52.7575	0.975	10.73	✗	✓	
DECam_J2323.5-5302	350.871	-53.0369	0.975	12.75	✗	✓	
DECam_J2324.8-5311	351.201	-53.1854	0.975	13.65	✗	✓	
DECam_J2320.4-5258	350.096	-52.9717	1.000	10.31	✗	✓	
DECam_J2319.8-5248	349.938	-52.8049	1.075	10.68	✗	✓	
DECam_J2322.4-5318	350.607	-53.2932	1.150	9.08	✗	✓	
DECam_J2321.1-5306	350.267	-53.0991	1.575	8.82	✗	✓	
DECam_J2318.9-5410	349.718	-54.1721	0.800	9.38	✗	✓	
DECam_J2321.1-5343	350.278	-53.7245	0.825	9.92	✗	✓	
DECam_J2322.6-5352	350.660	-53.8696	0.875	9.05	✗	✓	
DECam_J2318.9-5349	349.717	-53.8145	0.925	9.36	✗	✓	
DECam_J2319.3-5433	349.829	-54.5487	1.000	9.49	✗	✓	
DECam_J2323.5-5441	350.868	-54.6782	1.050	9.70	✗	✓	
DECam_J2322.6-5404	350.638	-54.0600	1.050	11.58	✗	✓	
DECam_J2320.7-5348	350.163	-53.7973	1.150	10.50	✗	✓	
DECam_J2329.7-5340	352.417	-53.6720	0.800	12.91	✗	✓	
DECam_J2331.2-5310	352.797	-53.1589	0.800	9.68	✗	✓	
DECam_J2331.9-5326	352.975	-53.4391	0.800	8.91	✗	✓	
DECam_J2330.2-5244	352.552	-52.7253	0.825	9.04	✗	✓	
DECam_J2327.9-5306	351.968	-53.0979	0.900	11.97	✗	✓	
DECam_J2326.5-5247	351.627	-52.7868	0.925	10.20	✗	✓	
DECam_J2328.4-5318	352.110	-53.2936	0.950	9.21	✗	✓	

Table A.1 —*Continued*

Cluster ID	R.A. (deg., J2000)	Dec (deg., J2000)	Redshift	ξ	RS	SBS	Other
DECam_J2327.5-5336	351.882	-53.5977	1.075	11.24	✗	✓	
DECam_J2332.2-5247	353.052	-52.7857	1.100	9.58	✗	✓	
DECam_J2331.9-5315	352.968	-53.2512	1.225	10.75	✗	✓	
DECam_J2329.6-5303	352.409	-53.0529	1.300	10.12	✗	✓	
DECam_J2325.9-5403	351.473	-54.0474	0.825	9.88	✗	✓	
DECam_J2327.0-5434	351.759	-54.5720	0.975	12.27	✗	✓	
DECam_J2329.2-5345	352.294	-53.7427	1.075	9.96	✗	✓	
DECam_J2327.6-5416	351.898	-54.2729	1.075	10.59	✗	✓	1
DECam_J2326.0-5424	351.504	-54.3923	1.125	10.61	✗	✓	
DECam_J2326.2-5446	351.549	-54.7655	0.900	10.20	✗	✓	
DECam_J2327.3-5504	351.821	-55.0709	0.925	15.31	✗	✓	
DECam_J2328.9-5521	352.229	-55.3579	0.925	9.93	✗	✓	
DECam_J2331.0-5529	352.748	-55.4894	0.975	10.40	✗	✓	
DECam_J2325.7-5525	351.422	-55.4245	1.025	10.07	✗	✓	
DECam_J2329.2-5502	352.301	-55.0402	1.100	10.65	✗	✓	
DECam_J2329.5-5539	352.371	-55.6462	1.575	8.85	✗	✓	
DECam_J2332.1-5546	353.031	-55.7699	0.800	9.43	✗	✓	
DECam_J2331.8-5633	352.942	-56.5525	0.875	12.48	✗	✓	
DECam_J2328.2-5549	352.039	-55.8244	0.875	11.62	✗	✓	1
DECam_J2327.4-5620	351.843	-56.3333	0.875	10.46	✗	✓	
DECam_J2325.3-5548	351.327	-55.8061	0.975	10.91	✗	✓	
DECam_J2330.7-5551	352.680	-55.8505	1.125	10.61	✗	✓	
DECam_J2329.0-5631	352.261	-56.5090	1.150	10.44	✗	✓	
DECam_J2327.8-5622	351.952	-56.3704	1.375	7.52	✗	✓	
DECam_J2325.2-5601	351.302	-56.0197	1.375	9.92	✗	✓	
DECam_J2328.0-5558	351.998	-55.9615	1.575	7.24	✗	✓	
DECam_J2330.8-5659	352.700	-56.9863	0.925	10.19	✗	✓	
DECam_J2325.3-5643	351.313	-56.7157	0.950	11.82	✗	✓	
DECam_J2331.6-5643	352.890	-56.7112	1.425	8.45	✗	✓	
DECam_J2325.8-5201	351.462	-52.0145	0.800	9.98	✗	✓	
DECam_J2329.0-5216	352.248	-52.2588	0.800	10.44	✗	✓	
DECam_J2329.8-5224	352.450	-52.3984	0.800	9.92	✗	✓	
DECam_J2325.8-5222	351.442	-52.3679	1.025	13.70	✗	✓	
DECam_J2328.2-5238	352.051	-52.6351	1.100	10.57	✗	✓	
DECam_J2330.8-5212	352.699	-52.1967	1.275	9.71	✗	✓	
DECam_J2331.9-5240	352.985	-52.6603	1.450	7.14	✗	✓	
DECam_J2332.6-5227	353.159	-52.4577	0.800	10.27	✗	✓	
DECam_J2336.6-5150	354.162	-51.8378	0.825	8.33	✗	✓	
DECam_J2335.5-5201	353.880	-52.0157	0.925	8.99	✗	✓	
DECam_J2338.0-5215	354.507	-52.2451	0.925	8.94	✗	✓	

Table A.1 —*Continued*

Cluster ID	R.A. (deg., J2000)	Dec (deg., J2000)	Redshift	ξ	RS	SBS	Other
DECam_J2335.1-5224	353.773	-52.3996	0.975	13.02	✗	✓	
DECam_J2336.6-5240	354.157	-52.6607	1.050	9.04	✗	✓	
DECam_J2335.2-5232	353.793	-52.5321	1.075	12.55	✗	✓	
DECam_J2337.7-5211	354.433	-52.1901	1.275	11.04	✗	✓	
DECam_J2332.6-5204	353.154	-52.0647	1.275	8.86	✗	✓	
DECam_J2336.4-5331	354.107	-53.5243	0.850	9.67	✗	✓	
DECam_J2337.3-5252	354.331	-52.8663	0.975	11.98	✗	✓	
DECam_J2334.7-5252	353.683	-52.8715	1.025	14.90	✗	✓	
DECam_J2336.2-5339	354.061	-53.6424	1.200	10.12	✗	✓	
DECam_J2336.7-5324	354.173	-53.3967	1.200	9.69	✗	✓	
DECam_J2332.6-5259	353.142	-52.9769	1.600	8.98	✗	✓	
DECam_J2337.2-5409	354.307	-54.1559	0.825	13.22	✗	✓	
DECam_J2332.7-5409	353.178	-54.1560	0.825	10.60	✗	✓	
DECam_J2335.4-5435	353.850	-54.5833	1.075	9.54	✗	✓	1
DECam_J2333.4-5346	353.356	-53.7642	1.100	9.33	✗	✓	
DECam_J2336.0-5425	353.995	-54.4236	1.125	10.21	✗	✓	
DECam_J2338.9-5407	354.724	-54.1131	1.250	9.21	✗	✓	
DECam_J2334.6-5538	353.645	-55.6383	0.900	9.88	✗	✓	
DECam_J2334.6-5527	353.643	-55.4549	0.950	9.99	✗	✓	
DECam_J2337.5-5505	354.376	-55.0794	0.950	9.08	✗	✓	
DECam_J2335.7-5522	353.930	-55.3669	0.975	9.56	✗	✓	
DECam_J2337.1-5523	354.263	-55.3799	0.975	9.28	✗	✓	
DECam_J2336.7-5451	354.173	-54.8567	1.025	15.07	✗	✓	
DECam_J2336.1-5629	354.013	-56.4851	0.825	8.61	✗	✓	
DECam_J2333.1-5611	353.274	-56.1905	0.925	9.78	✗	✓	
DECam_J2333.8-5550	353.455	-55.8280	0.950	9.12	✗	✓	
DECam_J2336.9-5615	354.219	-56.2422	1.050	8.46	✗	✓	
DECam_J2339.0-5602	354.750	-56.0287	1.050	11.57	✗	✓	
DECam_J2335.7-5610	353.915	-56.1723	1.250	8.71	✗	✓	
DECam_J2338.7-5546	354.665	-55.7678	1.325	12.79	✗	✓	
DECam_J2335.3-5622	353.834	-56.3707	1.400	8.45	✗	✓	
DECam_J2332.8-5618	353.198	-56.3007	1.550	8.26	✗	✓	
DECam_J2337.7-5651	354.434	-56.8466	0.875	10.66	✗	✓	
DECam_J2335.3-5702	353.835	-57.0259	1.100	11.19	✗	✓	
DECam_J2337.3-5706	354.333	-57.1062	1.125	9.71	✗	✓	
DECam_J2338.7-5146	354.679	-51.7670	0.800	7.74	✗	✓	
DECam_J2340.1-5215	355.031	-52.2550	0.850	7.53	✗	✓	
DECam_J2344.5-5240	356.130	-52.6743	0.900	9.00	✗	✓	
DECam_J2339.4-5225	354.853	-52.4210	0.925	8.70	✗	✓	
DECam_J2338.9-5242	354.729	-52.6941	0.975	9.54	✗	✓	

Table A.1 —*Continued*

Cluster ID	R.A. (deg., J2000)	Dec (deg., J2000)	Redshift	ξ	RS	SBS	Other
DECam_J2340.6-5243	355.144	-52.7129	1.000	11.23	✗	✓	
DECam_J2341.4-5228	355.341	-52.4687	1.150	10.31	✗	✓	
DECam_J2338.9-5336	354.722	-53.5922	0.800	8.75	✗	✓	
DECam_J2345.0-5310	356.241	-53.1683	0.825	9.96	✗	✓	
DECam_J2344.7-5324	356.181	-53.4072	0.850	8.77	✗	✓	
DECam_J2343.0-5304	355.757	-53.0728	0.875	7.87	✗	✓	
DECam_J2342.2-5317	355.559	-53.2852	0.900	9.41	✗	✓	
DECam_J2341.6-5329	355.392	-53.4782	1.100	9.76	✗	✓	
DECam_J2344.2-5342	356.041	-53.7017	0.850	14.63	✗	✓	
DECam_J2341.9-5439	355.487	-54.6564	0.925	10.16	✗	✓	
DECam_J2340.2-5420	355.060	-54.3397	1.075	10.49	✗	✓	
DECam_J2343.2-5426	355.804	-54.4386	1.100	10.41	✗	✓	
DECam_J2339.3-5430	354.831	-54.5006	1.150	9.74	✗	✓	
DECam_J2340.0-5410	355.002	-54.1615	1.150	8.44	✗	✓	
DECam_J2344.2-5417	356.041	-54.2913	1.250	8.56	✗	✓	
DECam_J2339.8-5454	354.943	-54.9049	0.950	9.73	✗	✓	
DECam_J2342.1-5504	355.537	-55.0708	1.000	9.46	✗	✓	
DECam_J2344.3-5519	356.085	-55.3140	1.050	8.53	✗	✓	
DECam_J2340.5-5506	355.114	-55.1016	1.250	13.56	✗	✓	
DECam_J2343.8-5638	355.945	-56.6346	0.850	10.89	✗	✓	
DECam_J2340.3-5550	355.072	-55.8284	0.875	10.15	✗	✓	
DECam_J2343.2-5560	355.794	-55.9995	0.925	11.30	✗	✓	
DECam_J2345.8-5618	356.439	-56.2957	0.925	12.41	✗	✓	
DECam_J2339.3-5605	354.825	-56.0810	1.125	8.51	✗	✓	
DECam_J2342.6-5643	355.646	-56.7190	0.850	13.07	✗	✓	
DECam_J2341.4-5652	355.349	-56.8664	1.325	9.79	✗	✓	
DECam_J2346.2-5233	356.558	-52.5471	0.975	11.23	✗	✓	
DECam_J2352.0-5325	357.993	-53.4171	0.875	10.47	✗	✓	
DECam_J2347.3-5323	356.823	-53.3817	0.925	9.76	✗	✓	
DECam_J2347.9-5302	356.987	-53.0409	1.100	10.02	✗	✓	
DECam_J2346.7-5301	356.666	-53.0177	1.475	13.82	✗	✓	
DECam_J2347.0-5407	356.738	-54.1219	0.800	10.65	✗	✓	
DECam_J2346.6-5353	356.642	-53.8804	0.950	9.85	✗	✓	
DECam_J2350.4-5351	357.597	-53.8435	1.000	9.17	✗	✓	
DECam_J2348.2-5426	357.043	-54.4276	1.300	10.44	✗	✓	
DECam_J2347.5-5540	356.863	-55.6639	0.950	13.46	✗	✓	
DECam_J2346.9-5529	356.721	-55.4831	0.975	10.00	✗	✓	
DECam_J2347.8-5506	356.960	-55.1075	0.975	10.27	✗	✓	
DECam_J2348.9-5449	357.216	-54.8136	1.275	9.72	✗	✓	
DECam_J2348.3-5606	357.069	-56.1001	0.800	15.38	✗	✓	

Table A.1 —*Continued*

Cluster ID	R.A. (deg., J2000)	Dec (deg., J2000)	Redshift	ξ	RS	SBS	Other
DECam_J2347.3-5625	356.825	-56.4182	1.250	12.96	✗	✓	
DECam_J2349.3-5709	357.336	-57.1552	0.850	8.07	✗	✓	
DECam_J2311.8-5410	347.951	-54.1713	0.425	15.89	✓	✗	
DECam_J2312.0-5434	347.993	-54.5684	0.525	11.37	✓	✗	
DECam_J2311.7-5348	347.927	-53.7933	0.550	13.12	✓	✗	
DECam_J2310.1-5348	347.528	-53.8004	0.625	13.00	✓	✗	
DECam_J2311.5-5418	347.870	-54.2977	0.775	9.82	✓	✗	
DECam_J2311.7-5319	347.924	-53.3193	0.400	15.36	✓	✗	
DECam_J2310.7-5253	347.664	-52.8789	0.425	13.82	✓	✗	
DECam_J239.4-5323	347.340	-53.3880	0.450	18.00	✓	✗	
DECam_J2311.9-5243	347.983	-52.7159	0.725	9.81	✓	✗	
DECam_J2311.6-5300	347.901	-53.0040	0.975	14.03	✓	✗	
DECam_J2311.6-5341	347.891	-53.6906	1.500	9.28	✓	✗	
DECam_J2315.2-5645	348.788	-56.7549	0.550	16.03	✓	✗	
DECam_J2317.5-5659	349.371	-56.9820	1.075	8.08	✓	✗	
DECam_J2312.0-5453	348.005	-54.8802	0.400	16.87	✓	✗	
DECam_J2317.0-5518	349.256	-55.3060	0.425	15.50	✓	✗	2
DECam_J2317.0-5455	349.254	-54.9154	0.425	15.63	✓	✗	1,2,3
DECam_J2314.2-5522	348.558	-55.3727	0.450	10.23	✓	✗	
DECam_J2318.0-5539	349.504	-55.6447	0.700	13.30	✓	✗	
DECam_J2314.7-5518	348.683	-55.3078	1.050	8.86	✓	✗	
DECam_J2317.7-5535	349.425	-55.5818	1.150	8.67	✓	✗	
DECam_J2313.9-5505	348.472	-55.0787	1.800	10.83	✓	✗	
DECam_J2316.5-5527	349.127	-55.4431	1.850	9.62	✓	✗	
DECam_J2318.0-5634	349.509	-56.5633	0.400	15.58	✓	✗	
DECam_J2314.9-5637	348.724	-56.6094	0.425	12.40	✓	✗	
DECam_J2314.9-5553	348.717	-55.8851	0.425	14.62	✓	✗	2
DECam_J2314.2-5555	348.556	-55.9125	0.775	13.10	✓	✗	2
DECam_J2317.3-5606	349.331	-56.0950	0.775	11.46	✓	✗	
DECam_J2315.5-5630	348.882	-56.4958	0.875	12.67	✓	✗	
DECam_J2317.3-5552	349.336	-55.8725	1.100	9.81	✓	✗	
DECam_J2315.6-5544	348.899	-55.7329	1.450	10.50	✓	✗	
DECam_J2317.9-5559	349.471	-55.9886	1.475	11.66	✓	✗	
DECam_J2315.0-5623	348.743	-56.3769	1.650	11.65	✓	✗	
DECam_J2316.5-5550	349.130	-55.8378	2.025	9.60	✓	✗	
DECam_J2317.5-5324	349.368	-53.4059	0.400	10.12	✓	✗	
DECam_J2314.6-5307	348.639	-53.1174	0.400	15.78	✓	✗	2
DECam_J2314.9-5339	348.723	-53.6449	0.525	10.83	✓	✗	
DECam_J2318.1-5247	349.517	-52.7815	0.525	24.13	✓	✗	1,2
DECam_J2312.6-5301	348.148	-53.0155	0.575	12.84	✓	✗	

Table A.1 —*Continued*

Cluster ID	R.A. (deg., J2000)	Dec (deg., J2000)	Redshift	ξ	RS	SBS	Other
DECam_J2313.4-5341	348.341	-53.6830	0.600	10.33	✓	✗	
DECam_J2313.9-5304	348.466	-53.0693	0.775	11.63	✓	✗	
DECam_J2317.7-5244	349.420	-52.7308	0.900	11.24	✓	✗	1
DECam_J2312.3-5320	348.081	-53.3375	1.000	10.61	✓	✗	
DECam_J2318.1-5303	349.515	-53.0444	1.100	10.10	✓	✗	
DECam_J2316.5-5243	349.116	-52.7195	1.175	9.58	✓	✗	
DECam_J2315.0-5301	348.760	-53.0191	1.225	9.96	✓	✗	
DECam_J2315.6-5327	348.911	-53.4424	1.475	10.19	✓	✗	
DECam_J2316.5-5258	349.129	-52.9634	1.550	11.85	✓	✗	
DECam_J2318.8-5258	349.691	-52.9684	1.775	8.43	✓	✗	
DECam_J2314.4-5245	348.597	-52.7485	1.950	8.06	✓	✗	
DECam_J2318.4-5319	349.591	-53.3086	2.000	8.72	✓	✗	
DECam_J2317.8-5437	349.462	-54.6124	0.425	14.35	✓	✗	
DECam_J2312.2-5356	348.041	-53.9262	0.425	13.32	✓	✗	
DECam_J2317.4-5359	349.345	-53.9815	0.425	16.52	✓	✗	1
DECam_J2313.7-5430	348.424	-54.4945	0.425	12.81	✓	✗	2
DECam_J2318.6-5345	349.657	-53.7439	0.525	10.57	✓	✗	
DECam_J2315.1-5345	348.782	-53.7490	0.850	12.48	✓	✗	
DECam_J2312.3-5418	348.066	-54.3018	0.875	11.89	✓	✗	
DECam_J2318.2-5354	349.547	-53.9079	0.875	11.50	✓	✗	
DECam_J2315.4-5415	348.838	-54.2560	0.900	9.38	✓	✗	
DECam_J2316.7-5424	349.166	-54.4040	0.950	10.41	✓	✗	
DECam_J2312.9-5353	348.222	-53.8854	1.050	8.91	✓	✗	
DECam_J2318.6-5408	349.640	-54.1392	1.075	9.99	✓	✗	
DECam_J2315.2-5439	348.798	-54.6467	1.125	16.06	✓	✗	
DECam_J2314.3-5404	348.585	-54.0722	1.300	9.74	✓	✗	
DECam_J2312.4-5353	348.091	-53.8776	1.450	9.15	✓	✗	
DECam_J2317.1-5344	349.266	-53.7380	1.500	10.88	✓	✗	
DECam_J2312.4-5437	348.111	-54.6171	1.525	9.18	✓	✗	
DECam_J2315.2-5352	348.789	-53.8683	1.650	10.05	✓	✗	
DECam_J2312.0-5350	348.009	-53.8375	1.775	8.92	✓	✗	
DECam_J2314.6-5413	348.656	-54.2085	1.950	8.84	✓	✗	
DECam_J2317.0-5411	349.240	-54.1829	2.025	7.92	✓	✗	
DECam_J2316.8-5212	349.205	-52.1936	0.425	16.15	✓	✗	
DECam_J2315.2-5234	348.800	-52.5596	0.550	28.14	✓	✗	2
DECam_J2319.0-5152	349.752	-51.8685	0.550	17.79	✓	✗	2
DECam_J2318.7-5239	349.679	-52.6550	0.600	13.06	✓	✗	
DECam_J2316.8-5226	349.192	-52.4258	0.750	11.83	✓	✗	
DECam_J2319.2-5148	349.792	-51.7972	1.100	8.43	✓	✗	
DECam_J2319.0-5210	349.745	-52.1623	1.100	8.10	✓	✗	

Table A.1 —*Continued*

Cluster ID	R.A. (deg., J2000)	Dec (deg., J2000)	Redshift	ξ	RS	SBS	Other
DECam_J2316.9-5232	349.227	-52.5269	1.150	13.53	✓	✗	
DECam_J2313.9-5235	348.481	-52.5844	1.975	10.30	✓	✗	
DECam_J2318.9-5243	349.718	-52.7089	2.125	6.52	✓	✗	
DECam_J2319.1-5506	349.773	-55.0935	0.400	13.68	✓	✗	
DECam_J2322.0-5446	350.500	-54.7602	0.450	34.97	✓	✗	1,2
DECam_J2319.1-5447	349.776	-54.7784	0.450	13.76	✓	✗	
DECam_J2324.5-5529	351.124	-55.4824	0.600	13.59	✓	✗	
DECam_J2324.0-5502	351.007	-55.0304	0.650	15.57	✓	✗	1,2
DECam_J2320.9-5503	350.225	-55.0425	0.875	9.91	✓	✗	
DECam_J2323.8-5519	350.958	-55.3163	0.900	12.62	✓	✗	
DECam_J2322.7-5537	350.669	-55.6243	0.975	11.25	✓	✗	
DECam_J2318.8-5458	349.707	-54.9590	1.475	10.60	✓	✗	
DECam_J2320.4-5529	350.100	-55.4877	1.500	8.82	✓	✗	
DECam_J2321.6-5536	350.402	-55.5953	1.800	8.88	✓	✗	
DECam_J2323.1-5444	350.781	-54.7327	1.825	9.35	✓	✗	
DECam_J2324.3-5528	351.087	-55.4610	1.975	9.08	✓	✗	
DECam_J2321.4-5457	350.345	-54.9527	2.025	7.46	✓	✗	
DECam_J2322.4-5534	350.604	-55.5711	2.125	7.84	✓	✗	
DECam_J2318.3-5550	349.587	-55.8369	0.400	12.25	✓	✗	1,2
DECam_J2320.3-5542	350.077	-55.7043	0.425	16.73	✓	✗	
DECam_J2321.2-5560	350.307	-55.9946	0.425	13.89	✓	✗	
DECam_J2324.0-5628	351.010	-56.4725	0.450	15.87	✓	✗	
DECam_J2319.5-5639	349.869	-56.6436	0.500	21.99	✓	✗	1
DECam_J2318.8-5617	349.706	-56.2875	0.600	25.01	✓	✗	1,2
DECam_J2322.7-5549	350.679	-55.8210	0.650	15.21	✓	✗	2
DECam_J2322.4-5617	350.605	-56.2891	0.750	15.42	✓	✗	
DECam_J2324.2-5610	351.050	-56.1711	0.875	13.81	✓	✗	
DECam_J2324.0-5628	351.005	-56.4608	0.950	10.54	✓	✗	
DECam_J2318.2-5620	349.550	-56.3363	1.000	13.33	✓	✗	
DECam_J2324.4-5550	351.091	-55.8321	1.050	10.61	✓	✗	
DECam_J2318.5-5604	349.625	-56.0712	1.100	9.78	✓	✗	
DECam_J2323.2-5560	350.810	-55.9946	1.175	10.15	✓	✗	
DECam_J2322.4-5607	350.588	-56.1144	1.200	15.47	✓	✗	
DECam_J2323.6-5619	350.894	-56.3139	1.275	9.58	✓	✗	
DECam_J2323.0-5608	350.756	-56.1383	1.625	8.64	✓	✗	
DECam_J2321.7-5611	350.437	-56.1839	1.725	9.36	✓	✗	
DECam_J2321.6-5634	350.401	-56.5647	1.925	9.02	✓	✗	
DECam_J2322.9-5559	350.727	-55.9813	2.000	11.22	✓	✗	
DECam_J2320.1-5650	350.025	-56.8328	0.425	12.41	✓	✗	
DECam_J2319.0-5709	349.738	-57.1523	0.425	14.00	✓	✗	

Table A.1 —*Continued*

Cluster ID	R.A. (deg., J2000)	Dec (deg., J2000)	Redshift	ξ	RS	SBS	Other
DECam_J2323.6-5658	350.890	-56.9742	0.525	16.13	✓	✗	
DECam_J2322.2-5645	350.560	-56.7513	0.575	10.05	✓	✗	
DECam_J2318.1-5646	349.533	-56.7722	0.675	14.01	✓	✗	
DECam_J2320.0-5652	350.009	-56.8672	0.925	10.80	✓	✗	
DECam_J2317.9-5702	349.474	-57.0303	0.975	12.49	✓	✗	
DECam_J2318.4-5644	349.590	-56.7336	1.125	12.49	✓	✗	
DECam_J2324.5-5648	351.123	-56.7951	1.650	10.92	✓	✗	
DECam_J2322.8-5655	350.708	-56.9178	1.900	9.24	✓	✗	
DECam_J2317.8-5651	349.455	-56.8552	2.000	9.77	✓	✗	
DECam_J2325.0-5230	351.238	-52.5025	0.400	16.63	✓	✗	
DECam_J2321.6-5223	350.407	-52.3866	0.400	11.59	✓	✗	
DECam_J2321.9-5159	350.469	-51.9850	0.425	15.38	✓	✗	
DECam_J2324.2-5201	351.055	-52.0098	0.425	9.90	✓	✗	
DECam_J2319.4-5152	349.843	-51.8739	0.475	12.60	✓	✗	2
DECam_J2320.3-5244	350.065	-52.7322	0.550	13.29	✓	✗	
DECam_J2319.5-5218	349.887	-52.3007	0.550	16.48	✓	✗	
DECam_J2325.4-5140	351.357	-51.6602	0.600	10.70	✓	✗	
DECam_J2325.1-5224	351.272	-52.3960	0.775	17.73	✓	✗	
DECam_J2320.5-5234	350.113	-52.5625	0.875	14.38	✓	✗	1
DECam_J2325.0-5236	351.253	-52.6019	1.050	10.40	✓	✗	
DECam_J2323.2-5146	350.791	-51.7637	1.075	9.98	✓	✗	
DECam_J2323.6-5211	350.893	-52.1813	1.125	8.75	✓	✗	
DECam_J2322.5-5232	350.619	-52.5337	1.175	10.26	✓	✗	
DECam_J2324.0-5238	350.993	-52.6306	1.350	9.70	✓	✗	
DECam_J2323.0-5156	350.757	-51.9371	1.375	9.39	✓	✗	
DECam_J2319.4-5159	349.849	-51.9814	1.525	9.17	✓	✗	
DECam_J2325.7-5214	351.423	-52.2338	1.575	9.38	✓	✗	
DECam_J2320.1-5145	350.035	-51.7445	1.575	7.71	✓	✗	
DECam_J2319.7-5210	349.932	-52.1658	1.575	7.80	✓	✗	
DECam_J2322.8-5222	350.696	-52.3602	1.750	12.71	✓	✗	
DECam_J2319.0-5341	349.758	-53.6834	0.400	11.52	✓	✗	
DECam_J2322.4-5244	350.612	-52.7343	0.400	13.07	✓	✗	1
DECam_J2324.5-5252	351.116	-52.8584	0.425	11.85	✓	✗	
DECam_J2322.9-5314	350.720	-53.2251	0.425	16.34	✓	✗	
DECam_J2325.5-5326	351.386	-53.4257	0.425	20.24	✓	✗	
DECam_J2319.6-5309	349.895	-53.1576	0.500	10.90	✓	✗	
DECam_J2320.6-5245	350.145	-52.7498	0.575	11.34	✓	✗	
DECam_J2320.1-5338	350.022	-53.6257	1.050	13.56	✓	✗	
DECam_J2321.0-5258	350.249	-52.9649	1.050	11.17	✓	✗	
DECam_J2324.0-5247	350.992	-52.7837	1.075	10.16	✓	✗	

Table A.1 —*Continued*

Cluster ID	R.A. (deg., J2000)	Dec (deg., J2000)	Redshift	ξ	RS	SBS	Other
DECam_J2323.0-5328	350.739	-53.4624	1.200	10.46	✓	✗	
DECam_J2320.6-5313	350.148	-53.2156	1.375	8.24	✓	✗	
DECam_J2320.1-5251	350.015	-52.8508	1.425	8.71	✓	✗	
DECam_J2321.7-5323	350.425	-53.3822	1.425	10.10	✓	✗	
DECam_J2322.1-5304	350.532	-53.0646	1.650	8.45	✓	✗	
DECam_J2325.5-5342	351.368	-53.6942	1.800	9.73	✓	✗	
DECam_J2321.5-5317	350.380	-53.2895	1.800	8.10	✓	✗	
DECam_J2321.5-5332	350.365	-53.5339	1.900	10.38	✓	✗	
DECam_J2324.8-5256	351.195	-52.9409	1.975	8.88	✓	✗	
DECam_J2319.2-5405	349.791	-54.0871	0.400	17.58	✓	✗	1,2
DECam_J2322.2-5428	350.548	-54.4705	0.400	14.75	✓	✗	2
DECam_J2319.8-5350	349.961	-53.8404	0.450	14.06	✓	✗	
DECam_J2325.5-5441	351.372	-54.6860	0.575	13.78	✓	✗	
DECam_J2325.5-5412	351.384	-54.2013	0.575	13.62	✓	✗	
DECam_J2322.1-5422	350.515	-54.3630	0.775	11.99	✓	✗	
DECam_J2320.0-5425	349.996	-54.4123	0.800	16.10	✓	✗	
DECam_J2321.7-5438	350.423	-54.6255	0.850	9.64	✓	✗	
DECam_J2320.9-5414	350.220	-54.2269	0.875	9.46	✓	✗	
DECam_J2319.1-5415	349.764	-54.2425	0.975	9.24	✓	✗	
DECam_J2321.1-5355	350.284	-53.9108	1.075	11.24	✓	✗	
DECam_J2323.4-5426	350.853	-54.4407	1.075	10.37	✓	✗	
DECam_J2322.3-5350	350.565	-53.8407	1.150	9.76	✓	✗	
DECam_J2319.6-5358	349.894	-53.9645	1.450	10.65	✓	✗	
DECam_J2324.9-5417	351.236	-54.2773	1.450	10.25	✓	✗	
DECam_J2324.9-5442	351.234	-54.6957	1.475	9.88	✓	✗	
DECam_J2322.6-5345	350.646	-53.7465	1.500	9.51	✓	✗	
DECam_J2320.9-5344	350.228	-53.7361	2.000	7.76	✓	✗	
DECam_J2320.7-5358	350.179	-53.9649	2.000	9.21	✓	✗	
DECam_J2322.6-5408	350.661	-54.1283	2.025	11.20	✓	✗	
DECam_J2318.9-5408	349.713	-54.1330	2.125	8.65	✓	✗	
DECam_J2327.9-5244	351.976	-52.7334	0.400	11.43	✓	✗	
DECam_J2325.7-5244	351.433	-52.7312	0.450	9.46	✓	✗	
DECam_J2326.7-5256	351.671	-52.9271	0.450	11.52	✓	✗	
DECam_J2331.7-5307	352.927	-53.1099	0.450	14.66	✓	✗	1
DECam_J2329.2-5320	352.297	-53.3267	0.450	22.24	✓	✗	
DECam_J2328.8-5339	352.202	-53.6490	0.550	18.01	✓	✗	
DECam_J2329.4-5254	352.340	-52.8948	0.600	12.55	✓	✗	
DECam_J2327.9-5323	351.978	-53.3904	0.725	15.03	✓	✗	
DECam_J2326.3-5313	351.566	-53.2110	0.925	14.36	✓	✗	
DECam_J2328.2-5301	352.044	-53.0092	0.950	11.12	✓	✗	

Table A.1 —*Continued*

Cluster ID	R.A. (deg., J2000)	Dec (deg., J2000)	Redshift	ξ	RS	SBS	Other
DECam_J2332.1-5304	353.019	-53.0680	1.125	8.81	✓	✗	
DECam_J2329.6-5330	352.407	-53.5008	1.350	9.25	✓	✗	
DECam_J2326.5-5325	351.627	-53.4098	1.375	8.77	✓	✗	
DECam_J2332.3-5334	353.070	-53.5640	1.375	11.34	✓	✗	
DECam_J2331.2-5332	352.796	-53.5374	1.475	11.76	✓	✗	
DECam_J2330.4-5254	352.592	-52.8996	1.650	9.52	✓	✗	
DECam_J2327.0-5304	351.749	-53.0635	1.875	9.02	✓	✗	
DECam_J2329.0-5331	352.245	-53.5212	2.125	9.25	✓	✗	
DECam_J2330.4-5322	352.599	-53.3607	2.125	9.38	✓	✗	
DECam_J2332.6-5400	353.142	-54.0022	0.425	10.66	✓	✗	1,2,3
DECam_J2330.5-5353	352.618	-53.8756	0.450	14.73	✓	✗	
DECam_J2326.0-5439	351.498	-54.6511	0.475	13.74	✓	✗	
DECam_J2326.2-5344	351.539	-53.7277	0.475	9.76	✓	✗	
DECam_J2330.1-5415	352.526	-54.2452	0.475	13.47	✓	✗	1,2
DECam_J2328.0-5404	352.008	-54.0653	0.600	15.04	✓	✗	
DECam_J2329.5-5422	352.375	-54.3586	0.775	11.58	✓	✗	
DECam_J2328.7-5347	352.183	-53.7913	0.825	10.48	✓	✗	1
DECam_J2328.6-5442	352.159	-54.6981	0.900	9.44	✓	✗	
DECam_J2331.9-5432	352.964	-54.5393	1.075	9.54	✓	✗	
DECam_J2330.0-5346	352.512	-53.7681	1.075	10.35	✓	✗	
DECam_J2332.2-5404	353.059	-54.0648	1.200	9.66	✓	✗	
DECam_J2330.9-5402	352.715	-54.0399	1.225	10.36	✓	✗	
DECam_J2327.3-5414	351.825	-54.2388	1.475	10.22	✓	✗	
DECam_J2331.3-5424	352.827	-54.3991	1.650	10.14	✓	✗	
DECam_J2327.0-5422	351.760	-54.3656	2.125	10.24	✓	✗	
DECam_J2331.1-5526	352.775	-55.4411	0.425	13.04	✓	✗	
DECam_J2326.6-5502	351.657	-55.0258	0.475	28.36	✓	✗	1,2
DECam_J2326.3-5523	351.573	-55.3890	0.675	18.17	✓	✗	1,2
DECam_J2330.5-5541	352.622	-55.6796	0.700	11.92	✓	✗	
DECam_J2329.7-5506	352.421	-55.0919	1.050	9.91	✓	✗	
DECam_J2331.4-5441	352.859	-54.6840	1.275	10.35	✓	✗	
DECam_J2328.9-5539	352.224	-55.6521	1.475	8.63	✓	✗	
DECam_J2327.8-5454	351.944	-54.8961	1.475	9.16	✓	✗	
DECam_J2330.7-5501	352.686	-55.0109	1.550	8.43	✓	✗	
DECam_J2327.7-5540	351.930	-55.6598	1.825	11.10	✓	✗	
DECam_J2327.3-5521	351.813	-55.3517	1.850	8.74	✓	✗	
DECam_J2328.1-5448	352.024	-54.7925	1.975	9.09	✓	✗	
DECam_J2325.5-5549	351.366	-55.8174	0.400	11.22	✓	✗	
DECam_J2332.1-5552	353.021	-55.8641	0.400	14.51	✓	✗	
DECam_J2328.0-5631	352.009	-56.5151	0.425	11.87	✓	✗	

Table A.1 —*Continued*

Cluster ID	R.A. (deg., J2000)	Dec (deg., J2000)	Redshift	ξ	RS	SBS	Other
DECam_J2331.6-5639	352.896	-56.6529	0.475	15.51	✓	✗	
DECam_J2325.3-5630	351.326	-56.5071	0.475	9.94	✓	✗	
DECam_J2329.9-5608	352.477	-56.1389	0.500	22.92	✓	✗	1,2
DECam_J2332.3-5612	353.064	-56.2049	0.550	16.63	✓	✗	
DECam_J2328.8-5547	352.205	-55.7830	0.575	12.65	✓	✗	
DECam_J2326.1-5603	351.525	-56.0583	0.750	15.10	✓	✗	
DECam_J2329.5-5626	352.380	-56.4273	0.950	12.32	✓	✗	
DECam_J2330.4-5557	352.606	-55.9484	0.950	12.06	✓	✗	
DECam_J2330.7-5617	352.671	-56.2840	1.025	11.83	✓	✗	
DECam_J2325.2-5638	351.300	-56.6346	1.100	9.60	✓	✗	
DECam_J2328.5-5617	352.119	-56.2759	1.325	9.72	✓	✗	
DECam_J2331.6-5551	352.894	-55.8465	1.400	11.12	✓	✗	
DECam_J2328.0-5639	352.009	-56.6508	1.575	8.20	✓	✗	
DECam_J2327.1-5543	351.777	-55.7165	1.600	8.22	✓	✗	
DECam_J2329.5-5623	352.383	-56.3790	1.800	7.73	✓	✗	
DECam_J2330.1-5546	352.532	-55.7607	2.025	7.92	✓	✗	
DECam_J2329.2-5607	352.311	-56.1186	2.125	6.57	✓	✗	
DECam_J2331.4-5552	352.851	-55.8594	2.125	6.54	✓	✗	
DECam_J2331.2-5645	352.808	-56.7446	0.400	16.14	✓	✗	
DECam_J2327.7-5643	351.929	-56.7140	0.400	12.07	✓	✗	
DECam_J2325.5-5659	351.377	-56.9788	0.425	13.58	✓	✗	
DECam_J2330.9-5711	352.725	-57.1827	0.600	17.45	✓	✗	
DECam_J2332.0-5642	353.009	-56.6949	0.725	11.35	✓	✗	
DECam_J2325.3-5645	351.334	-56.7515	0.750	18.72	✓	✗	
DECam_J2329.9-5647	352.482	-56.7801	0.975	11.42	✓	✗	
DECam_J2325.4-5657	351.353	-56.9492	1.025	10.43	✓	✗	
DECam_J2330.0-5703	352.502	-57.0444	1.175	12.24	✓	✗	
DECam_J2332.2-5702	353.038	-57.0305	1.450	8.81	✓	✗	
DECam_J2327.9-5643	351.986	-56.7085	1.650	9.60	✓	✗	
DECam_J2332.1-5240	353.018	-52.6674	0.400	14.69	✓	✗	
DECam_J2330.2-5217	352.551	-52.2908	0.400	16.25	✓	✗	
DECam_J2327.4-5228	351.862	-52.4603	0.400	15.81	✓	✗	
DECam_J2329.7-5153	352.416	-51.8848	0.425	12.00	✓	✗	
DECam_J2332.0-5150	353.006	-51.8312	0.525	12.78	✓	✗	
DECam_J2331.8-5205	352.942	-52.0880	0.650	20.82	✓	✗	2
DECam_J2329.2-5230	352.304	-52.4929	0.775	17.52	✓	✗	1
DECam_J2326.9-5214	351.728	-52.2350	0.975	12.74	✓	✗	
DECam_J2326.0-5222	351.496	-52.3747	1.075	12.36	✓	✗	
DECam_J2332.0-5154	352.997	-51.9026	1.100	11.10	✓	✗	
DECam_J2331.5-5204	352.884	-52.0657	1.275	10.89	✓	✗	

Table A.1 —*Continued*

Cluster ID	R.A. (deg., J2000)	Dec (deg., J2000)	Redshift	ξ	RS	SBS	Other
DECam_J2325.8-5243	351.444	-52.7143	1.350	9.79	✓	✗	
DECam_J2331.3-5236	352.814	-52.5918	1.450	9.37	✓	✗	
DECam_J2330.9-5215	352.724	-52.2462	1.450	9.86	✓	✗	
DECam_J2326.4-5159	351.602	-51.9786	1.475	11.74	✓	✗	
DECam_J2330.6-5158	352.659	-51.9653	1.525	9.09	✓	✗	
DECam_J2325.6-5222	351.412	-52.3675	1.550	8.41	✓	✗	
DECam_J2326.5-5224	351.637	-52.4024	2.025	7.17	✓	✗	
DECam_J2330.4-5151	352.608	-51.8480	2.125	6.35	✓	✗	
DECam_J2326.8-5205	351.708	-52.0756	2.125	5.82	✓	✗	
DECam_J2338.5-5204	354.617	-52.0716	0.400	15.60	✓	✗	2
DECam_J2333.3-5151	353.313	-51.8467	0.600	11.79	✓	✗	
DECam_J2333.5-5215	353.381	-52.2500	0.600	14.73	✓	✗	1,2
DECam_J2333.5-5240	353.374	-52.6597	0.600	16.03	✓	✗	2
DECam_J2335.7-5152	353.934	-51.8701	0.650	22.25	✓	✗	2
DECam_J2337.1-5221	354.286	-52.3533	0.775	10.47	✓	✗	
DECam_J2338.6-5221	354.649	-52.3550	0.925	7.77	✓	✗	
DECam_J2335.0-5159	353.739	-51.9761	1.100	8.23	✓	✗	
DECam_J2336.0-5234	353.996	-52.5606	1.150	10.46	✓	✗	
DECam_J2335.3-5146	353.820	-51.7673	1.200	9.40	✓	✗	
DECam_J2338.1-5236	354.537	-52.6040	1.225	10.54	✓	✗	
DECam_J2337.4-5216	354.344	-52.2676	1.225	12.75	✓	✗	
DECam_J2332.6-5227	353.155	-52.4560	1.275	8.85	✓	✗	
DECam_J2332.8-5213	353.209	-52.2173	1.325	9.91	✓	✗	
DECam_J2335.4-5155	353.854	-51.9159	1.550	11.81	✓	✗	
DECam_J2333.8-5156	353.439	-51.9330	1.575	10.79	✓	✗	
DECam_J2336.8-5150	354.193	-51.8386	1.625	7.95	✓	✗	
DECam_J2337.0-5233	354.247	-52.5449	1.725	8.98	✓	✗	
DECam_J2332.7-5150	353.175	-51.8382	1.825	7.06	✓	✗	
DECam_J2336.1-5215	354.031	-52.2478	1.850	7.32	✓	✗	
DECam_J2335.6-5338	353.894	-53.6298	0.400	10.79	✓	✗	
DECam_J2338.7-5327	354.680	-53.4552	0.425	11.93	✓	✗	
DECam_J2334.3-5316	353.572	-53.2669	0.450	13.48	✓	✗	
DECam_J2337.9-5311	354.484	-53.1885	0.550	17.13	✓	✗	2
DECam_J2336.6-5244	354.144	-52.7310	0.625	18.37	✓	✗	1,2
DECam_J2338.2-5337	354.551	-53.6117	0.875	10.91	✓	✗	
DECam_J2338.3-5321	354.581	-53.3549	1.000	12.46	✓	✗	
DECam_J2337.4-5254	354.341	-52.8948	1.075	8.96	✓	✗	
DECam_J2335.6-5306	353.898	-53.1064	1.075	9.92	✓	✗	
DECam_J2336.0-5336	353.996	-53.5993	1.300	11.65	✓	✗	
DECam_J2338.0-5303	354.488	-53.0451	1.425	9.88	✓	✗	

Table A.1 —*Continued*

Cluster ID	R.A. (deg., J2000)	Dec (deg., J2000)	Redshift	ξ	RS	SBS	Other
DECam_J2332.4-5257	353.109	-52.9570	1.700	9.92	✓	✗	
DECam_J2337.8-5334	354.439	-53.5589	1.725	8.16	✓	✗	
DECam_J2334.3-5300	353.565	-53.0060	1.725	7.97	✓	✗	
DECam_J2337.7-5321	354.413	-53.3437	1.800	9.40	✓	✗	
DECam_J2333.1-5311	353.280	-53.1769	2.125	11.38	✓	✗	
DECam_J2338.6-5438	354.656	-54.6327	0.425	17.48	✓	✗	1,2
DECam_J2333.3-5422	353.324	-54.3617	0.425	12.60	✓	✗	
DECam_J2336.8-5347	354.194	-53.7901	0.450	21.93	✓	✗	1,2
DECam_J2332.5-5359	353.121	-53.9905	0.475	25.02	✓	✗	1,2,3
DECam_J2337.0-5424	354.243	-54.4065	0.575	18.53	✓	✗	2
DECam_J2336.2-5440	354.049	-54.6704	0.600	10.05	✓	✗	
DECam_J2338.5-5411	354.634	-54.1831	0.675	15.65	✓	✗	
DECam_J2333.8-5347	353.454	-53.7881	0.725	9.46	✓	✗	
DECam_J2335.9-5415	353.967	-54.2538	0.925	10.90	✓	✗	
DECam_J2337.6-5354	354.401	-53.8999	0.950	8.74	✓	✗	
DECam_J2336.0-5427	353.997	-54.4578	1.050	9.80	✓	✗	
DECam_J2337.1-5439	354.280	-54.6494	1.075	11.16	✓	✗	
DECam_J2338.5-5441	354.632	-54.6757	1.100	9.98	✓	✗	
DECam_J2337.7-5422	354.433	-54.3686	1.225	10.34	✓	✗	
DECam_J2333.5-5414	353.367	-54.2298	1.300	9.76	✓	✗	
DECam_J2333.0-5350	353.240	-53.8261	1.325	9.83	✓	✗	
DECam_J2336.6-5342	354.149	-53.7083	1.400	14.79	✓	✗	
DECam_J2337.6-5400	354.404	-54.0059	1.425	10.48	✓	✗	
DECam_J2337.7-5435	354.413	-54.5821	1.450	10.00	✓	✗	
DECam_J2338.5-5346	354.621	-53.7639	1.700	8.46	✓	✗	
DECam_J2336.5-5345	354.124	-53.7441	1.800	9.64	✓	✗	
DECam_J2332.3-5443	353.067	-54.7145	0.400	18.01	✓	✗	1,2
DECam_J2337.6-5445	354.411	-54.7554	0.400	13.80	✓	✗	
DECam_J2334.8-5517	353.698	-55.2757	0.425	17.67	✓	✗	1
DECam_J2338.3-5540	354.570	-55.6640	0.550	21.04	✓	✗	1,2
DECam_J2339.0-5500	354.745	-55.0009	0.600	13.62	✓	✗	
DECam_J2333.6-5538	353.411	-55.6355	0.750	17.29	✓	✗	1,2
DECam_J2335.7-5512	353.925	-55.1992	0.950	12.14	✓	✗	
DECam_J2336.6-5450	354.146	-54.8323	1.150	13.53	✓	✗	
DECam_J2337.0-5541	354.246	-55.6839	1.175	9.87	✓	✗	
DECam_J2333.6-5521	353.392	-55.3513	1.200	8.89	✓	✗	
DECam_J2337.8-5517	354.443	-55.2872	1.300	10.48	✓	✗	
DECam_J2332.2-5529	353.055	-55.4864	1.525	10.40	✓	✗	
DECam_J2335.7-5459	353.913	-54.9755	1.525	8.75	✓	✗	
DECam_J2336.2-5531	354.048	-55.5194	1.650	8.31	✓	✗	

Table A.1 —*Continued*

Cluster ID	R.A. (deg., J2000)	Dec (deg., J2000)	Redshift	ξ	RS	SBS	Other
DECam_J2337.2-5443	354.301	-54.7159	1.650	10.85	✓	✗	
DECam_J2333.7-5446	353.421	-54.7708	1.650	8.63	✓	✗	
DECam_J2333.7-5501	353.433	-55.0165	1.650	8.80	✓	✗	
DECam_J2333.7-5530	353.435	-55.5036	1.775	7.96	✓	✗	
DECam_J2332.4-5640	353.112	-56.6675	0.400	10.84	✓	✗	
DECam_J2332.4-5603	353.101	-56.0462	0.400	24.61	✓	✗	1
DECam_J2332.4-5623	353.099	-56.3899	0.400	14.71	✓	✗	
DECam_J2335.1-5629	353.778	-56.4820	0.400	13.97	✓	✗	
DECam_J2339.3-5550	354.818	-55.8373	0.425	13.03	✓	✗	1,2
DECam_J2338.0-5611	354.508	-56.1870	0.425	15.07	✓	✗	2
DECam_J2337.7-5630	354.421	-56.5076	0.425	13.11	✓	✗	
DECam_J2336.3-5554	354.086	-55.9061	0.600	15.26	✓	✗	2
DECam_J2334.4-5541	353.609	-55.6892	0.825	11.57	✓	✗	2
DECam_J2332.9-5640	353.224	-56.6630	0.900	8.98	✓	✗	
DECam_J2333.4-5554	353.350	-55.8917	0.925	9.59	✓	✗	
DECam_J2334.7-5557	353.671	-55.9455	0.925	9.22	✓	✗	
DECam_J2332.7-5544	353.167	-55.7395	1.025	10.03	✓	✗	
DECam_J2338.8-5560	354.698	-55.9945	1.200	11.08	✓	✗	
DECam_J2337.2-5544	354.291	-55.7259	1.200	12.82	✓	✗	
DECam_J2333.4-5640	353.340	-56.6712	1.325	10.73	✓	✗	
DECam_J2333.0-5629	353.238	-56.4913	1.325	9.03	✓	✗	
DECam_J2335.7-5631	353.917	-56.5120	1.375	10.46	✓	✗	
DECam_J2334.2-5630	353.542	-56.4988	1.575	8.79	✓	✗	
DECam_J2335.9-5545	353.971	-55.7464	1.750	10.23	✓	✗	
DECam_J2334.5-5542	353.623	-55.6999	1.800	8.32	✓	✗	
DECam_J2334.1-5557	353.520	-55.9507	1.875	8.92	✓	✗	
DECam_J2336.8-5626	354.191	-56.4349	1.975	8.85	✓	✗	
DECam_J2339.0-5612	354.752	-56.1921	2.025	8.67	✓	✗	
DECam_J2335.6-5705	353.911	-57.0776	0.425	13.08	✓	✗	
DECam_J2332.6-5654	353.155	-56.9024	0.425	13.13	✓	✗	
DECam_J2339.3-5649	354.817	-56.8196	0.450	8.73	✓	✗	2
DECam_J2332.4-5710	353.099	-57.1724	0.475	8.95	✓	✗	
DECam_J2336.0-5648	354.012	-56.8061	0.525	12.19	✓	✗	
DECam_J2337.4-5657	354.351	-56.9491	0.600	13.24	✓	✗	
DECam_J2338.2-5646	354.555	-56.7658	0.875	10.99	✓	✗	
DECam_J2335.0-5703	353.742	-57.0476	1.175	8.97	✓	✗	
DECam_J2337.4-5652	354.343	-56.8718	1.250	9.19	✓	✗	
DECam_J2334.9-5642	353.727	-56.7011	1.325	11.49	✓	✗	
DECam_J2333.2-5659	353.306	-56.9890	1.475	11.58	✓	✗	
DECam_J2339.5-5233	354.863	-52.5439	0.400	12.97	✓	✗	

Table A.1 —*Continued*

Cluster ID	R.A. (deg., J2000)	Dec (deg., J2000)	Redshift	ξ	RS	SBS	Other
DECam_J2338.8-5218	354.697	-52.2971	0.400	12.76	✓	✗	
DECam_J2341.9-5235	355.471	-52.5894	0.475	10.45	✓	✗	
DECam_J2338.9-5152	354.715	-51.8599	0.525	14.30	✓	✗	
DECam_J2345.2-5230	356.307	-52.4955	0.775	11.28	✓	✗	
DECam_J2339.8-5231	354.956	-52.5219	0.775	20.79	✓	✗	
DECam_J2340.7-5238	355.176	-52.6305	1.875	7.58	✓	✗	
DECam_J2340.7-5227	355.183	-52.4457	1.975	8.70	✓	✗	
DECam_J2339.4-5204	354.853	-52.0655	2.025	8.23	✓	✗	
DECam_J2340.2-5336	355.056	-53.5941	0.400	15.17	✓	✗	
DECam_J2340.1-5325	355.018	-53.4180	0.425	12.05	✓	✗	
DECam_J2343.7-5258	355.937	-52.9678	0.550	12.28	✓	✗	
DECam_J2341.9-5308	355.465	-53.1330	0.575	22.29	✓	✗	1,2
DECam_J2339.5-5245	354.881	-52.7516	0.600	12.43	✓	✗	
DECam_J2339.1-5335	354.772	-53.5852	0.925	8.93	✓	✗	
DECam_J2342.7-5322	355.675	-53.3747	1.375	13.66	✓	✗	
DECam_J2340.8-5253	355.206	-52.8860	1.800	10.82	✓	✗	
DECam_J2343.9-5307	355.978	-53.1236	1.825	10.22	✓	✗	
DECam_J2344.7-5337	356.175	-53.6211	1.875	7.96	✓	✗	
DECam_J2344.6-5248	356.146	-52.7959	1.975	7.90	✓	✗	
DECam_J2343.2-5253	355.791	-52.8806	2.125	8.56	✓	✗	
DECam_J2342.9-5441	355.718	-54.6765	0.400	14.27	✓	✗	
DECam_J2340.2-5344	355.048	-53.7262	0.400	13.77	✓	✗	
DECam_J2340.7-5432	355.167	-54.5311	0.400	15.01	✓	✗	
DECam_J2345.0-5431	356.248	-54.5197	0.500	14.27	✓	✗	1
DECam_J2345.8-5402	356.460	-54.0310	0.600	12.57	✓	✗	1,2
DECam_J2345.3-5351	356.329	-53.8544	0.650	20.90	✓	✗	
DECam_J2339.1-5420	354.787	-54.3326	0.675	14.80	✓	✗	
DECam_J2340.6-5441	355.141	-54.6782	0.725	10.46	✓	✗	2
DECam_J2343.6-5417	355.906	-54.2873	0.750	13.44	✓	✗	
DECam_J2342.7-5344	355.674	-53.7363	0.825	10.96	✓	✗	
DECam_J2345.4-5412	356.359	-54.2033	1.050	10.55	✓	✗	
DECam_J2340.1-5349	355.013	-53.8216	1.400	9.59	✓	✗	
DECam_J2341.3-5352	355.315	-53.8733	1.575	9.76	✓	✗	
DECam_J2345.4-5418	356.345	-54.3051	1.650	8.46	✓	✗	
DECam_J2342.0-5408	355.504	-54.1320	1.950	8.56	✓	✗	
DECam_J2340.1-5435	355.013	-54.5820	2.025	7.96	✓	✗	
DECam_J2342.7-5423	355.675	-54.3810	2.025	7.65	✓	✗	
DECam_J2345.3-5415	356.325	-54.2449	2.125	8.28	✓	✗	
DECam_J2340.0-5512	355.001	-55.2058	0.400	12.77	✓	✗	
DECam_J2340.5-5533	355.113	-55.5561	0.425	16.21	✓	✗	

Table A.1 —*Continued*

Cluster ID	R.A. (deg., J2000)	Dec (deg., J2000)	Redshift	ξ	RS	SBS	Other
DECam_J2344.5-5445	356.123	-54.7545	0.425	11.28	✓	✗	
DECam_J2342.5-5450	355.633	-54.8318	0.425	14.63	✓	✗	
DECam_J2342.7-5520	355.680	-55.3261	0.450	14.92	✓	✗	
DECam_J2345.9-5525	356.468	-55.4094	0.450	15.38	✓	✗	2
DECam_J2339.6-5446	354.903	-54.7590	0.900	13.57	✓	✗	
DECam_J2345.8-5520	356.449	-55.3322	0.925	10.10	✓	✗	
DECam_J2343.2-5539	355.803	-55.6520	0.950	9.67	✓	✗	
DECam_J2344.9-5451	356.220	-54.8537	1.075	10.44	✓	✗	
DECam_J2341.3-5444	355.326	-54.7363	1.100	10.43	✓	✗	
DECam_J2339.6-5446	354.903	-54.7585	1.200	10.03	✓	✗	
DECam_J2343.6-5537	355.905	-55.6099	1.400	8.42	✓	✗	
DECam_J2345.4-5515	356.359	-55.2568	1.450	10.14	✓	✗	
DECam_J2340.2-5504	355.054	-55.0644	1.475	7.80	✓	✗	
DECam_J2342.2-5454	355.539	-54.9016	1.500	6.96	✓	✗	
DECam_J2345.2-5538	356.311	-55.6393	1.575	7.91	✓	✗	
DECam_J2344.4-5529	356.095	-55.4815	1.825	5.90	✓	✗	
DECam_J2343.2-5518	355.788	-55.2922	2.025	6.24	✓	✗	
DECam_J2344.0-5444	355.999	-54.7358	2.025	8.50	✓	✗	
DECam_J2346.0-5641	356.501	-56.6871	0.475	11.76	✓	✗	
DECam_J2339.5-5550	354.871	-55.8374	0.500	18.63	✓	✗	1,2
DECam_J2342.6-5555	355.640	-55.9248	0.500	15.20	✓	✗	2
DECam_J2341.3-5604	355.317	-56.0653	0.525	14.37	✓	✗	1
DECam_J2342.7-5633	355.670	-56.5545	0.525	12.85	✓	✗	
DECam_J2344.1-5639	356.028	-56.6421	0.600	12.00	✓	✗	2
DECam_J2344.8-5617	356.197	-56.2914	0.675	25.22	✓	✗	1,2
DECam_J2346.3-5543	356.574	-55.7108	0.875	10.07	✓	✗	
DECam_J2340.8-5609	355.206	-56.1461	1.050	10.49	✓	✗	
DECam_J2342.3-5553	355.567	-55.8787	1.125	11.48	✓	✗	
DECam_J2339.6-5613	354.889	-56.2172	1.175	11.70	✓	✗	
DECam_J2340.2-5549	355.057	-55.8249	1.375	9.72	✓	✗	
DECam_J2344.6-5630	356.141	-56.5007	1.550	8.28	✓	✗	
DECam_J2341.0-5548	355.261	-55.8019	1.700	10.20	✓	✗	
DECam_J2344.9-5557	356.220	-55.9536	1.700	10.58	✓	✗	
DECam_J2339.9-5606	354.967	-56.1065	1.700	10.97	✓	✗	
DECam_J2342.4-5610	355.607	-56.1708	1.800	8.87	✓	✗	
DECam_J2346.3-5638	356.578	-56.6309	2.025	10.23	✓	✗	
DECam_J2345.3-5711	356.331	-57.1858	0.400	14.78	✓	✗	
DECam_J2343.2-5647	355.790	-56.7853	0.525	17.76	✓	✗	
DECam_J2340.6-5648	355.142	-56.7943	0.550	13.22	✓	✗	2
DECam_J2342.5-5704	355.624	-57.0610	0.750	12.47	✓	✗	2

Table A.1 —*Continued*

Cluster ID	R.A. (deg., J2000)	Dec (deg., J2000)	Redshift	ξ	RS	SBS	Other
DECam_J2340.2-5648	355.051	-56.8065	1.125	12.18	✓	✗	
DECam_J2343.6-5709	355.896	-57.1449	1.500	9.39	✓	✗	
DECam_J2346.9-5703	356.720	-57.0572	1.650	11.76	✓	✗	
DECam_J2340.2-5641	355.055	-56.6821	1.650	9.69	✓	✗	
DECam_J2348.5-5240	357.129	-52.6584	0.425	10.81	✓	✗	
DECam_J2346.0-5231	356.499	-52.5087	0.425	16.94	✓	✗	
DECam_J2346.9-5243	356.736	-52.7175	1.325	10.98	✓	✗	
DECam_J2346.3-5249	356.575	-52.8206	0.400	8.75	✓	✗	
DECam_J2348.7-5342	357.172	-53.6927	0.425	11.61	✓	✗	
DECam_J2349.8-5250	357.445	-52.8259	0.425	20.39	✓	✗	
DECam_J2351.1-5331	357.785	-53.5094	0.425	10.15	✓	✗	
DECam_J2345.6-5331	356.390	-53.5094	0.575	18.70	✓	✗	
DECam_J2350.9-5301	357.724	-53.0183	0.600	19.76	✓	✗	3
DECam_J2347.9-5317	356.972	-53.2797	0.775	16.71	✓	✗	
DECam_J2347.2-5259	356.797	-52.9864	0.925	9.64	✓	✗	
DECam_J2345.9-5311	356.471	-53.1774	1.250	10.98	✓	✗	
DECam_J2347.9-5250	356.970	-52.8338	1.475	11.40	✓	✗	
DECam_J2350.5-5312	357.616	-53.2078	1.500	11.87	✓	✗	
DECam_J2346.4-5311	356.601	-53.1809	1.700	8.16	✓	✗	
DECam_J2345.6-5337	356.406	-53.6118	1.900	8.09	✓	✗	
DECam_J2348.6-5415	357.145	-54.2425	0.500	11.90	✓	✗	
DECam_J2349.8-5404	357.440	-54.0596	0.525	11.77	✓	✗	2
DECam_J2346.0-5411	356.509	-54.1759	0.575	17.86	✓	✗	
DECam_J2346.3-5346	356.573	-53.7614	0.600	12.36	✓	✗	
DECam_J2347.7-5437	356.922	-54.6204	0.700	12.93	✓	✗	
DECam_J2347.7-5425	356.930	-54.4191	0.825	10.98	✓	✗	
DECam_J2350.1-5402	357.518	-54.0379	1.175	8.97	✓	✗	
DECam_J2346.1-5418	356.517	-54.2951	1.225	11.22	✓	✗	
DECam_J2350.5-5349	357.625	-53.8160	1.225	9.41	✓	✗	
DECam_J2348.1-5406	357.019	-54.0977	1.525	9.08	✓	✗	
DECam_J2345.9-5418	356.480	-54.3038	1.950	7.39	✓	✗	
DECam_J2348.4-5343	357.108	-53.7200	1.975	7.20	✓	✗	
DECam_J2347.5-5535	356.868	-55.5781	0.400	12.73	✓	✗	
DECam_J2349.7-5516	357.414	-55.2693	0.500	17.66	✓	✗	2
DECam_J2346.3-5456	356.575	-54.9349	0.575	12.01	✓	✗	2
DECam_J2346.3-5514	356.565	-55.2399	0.600	10.84	✓	✗	
DECam_J2346.3-5539	356.568	-55.6472	0.925	9.27	✓	✗	1,2
DECam_J2349.1-5527	357.277	-55.4551	0.975	9.05	✓	✗	
DECam_J2347.2-5457	356.797	-54.9428	1.100	9.18	✓	✗	
DECam_J2348.0-5444	356.995	-54.7412	1.150	12.17	✓	✗	

Table A.1 —*Continued*

Cluster ID	R.A. (deg., J2000)	Dec (deg., J2000)	Redshift	ξ	RS	SBS	Other
DECam_J2346.4-5533	356.610	-55.5460	1.475	9.60	✓	✗	
DECam_J2347.5-5525	356.874	-55.4209	1.525	10.10	✓	✗	
DECam_J2349.5-5533	357.372	-55.5561	1.575	10.37	✓	✗	
DECam_J2347.1-5442	356.777	-54.7061	1.650	8.67	✓	✗	
DECam_J2348.4-5533	357.102	-55.5580	1.975	7.58	✓	✗	
DECam_J2350.2-5637	357.540	-56.6158	0.400	13.14	✓	✗	
DECam_J2351.8-5556	357.940	-55.9266	0.400	14.45	✓	✗	
DECam_J2346.9-5615	356.719	-56.2531	0.400	13.26	✓	✗	
DECam_J2348.7-5622	357.186	-56.3652	0.400	12.23	✓	✗	
DECam_J2352.6-5627	358.157	-56.4467	0.400	14.57	✓	✗	
DECam_J2348.1-5602	357.031	-56.0283	0.500	28.46	✓	✗	1,2
DECam_J2354.0-5609	358.496	-56.1543	0.525	11.56	✓	✗	
DECam_J2349.4-5542	357.346	-55.6925	0.550	12.06	✓	✗	
DECam_J2347.1-5557	356.772	-55.9478	1.200	11.97	✓	✗	
DECam_J2350.2-5557	357.562	-55.9519	1.500	10.24	✓	✗	
DECam_J2348.9-5622	357.230	-56.3712	1.800	7.81	✓	✗	
DECam_J2348.8-5542	357.188	-55.7060	1.800	8.74	✓	✗	
DECam_J2349.4-5612	357.358	-56.1918	1.875	11.67	✓	✗	
DECam_J2351.5-5635	357.867	-56.5783	2.000	10.26	✓	✗	
DECam_J2349.2-5633	357.308	-56.5555	2.125	7.41	✓	✗	
DECam_J2351.0-5646	357.754	-56.7661	0.425	11.31	✓	✗	
DECam_J2349.2-5660	357.289	-56.9989	0.525	18.02	✓	✗	2
DECam_J2351.6-5641	357.910	-56.6861	1.025	9.05	✓	✗	
DECam_J2349.7-5655	357.415	-56.9183	1.150	8.90	✓	✗	
DECam_J2348.6-5711	357.154	-57.1797	1.175	8.28	✓	✗	
DECam_J2348.7-5644	357.186	-56.7270	1.175	9.94	✓	✗	
DECam_J2348.6-5705	357.154	-57.0845	1.500	10.39	✓	✗	
DECam_J2348.6-5707	357.146	-57.1243	1.850	8.19	✓	✗	

References:
[1] X-ray catalogue Pierre et al. (in preparation);
[2] optical BCS catalogue Bleem et al. (2014a);
[3] Sunyaev-Zel'dovich effect catalogue Bleem et al. (2014b);
[4] optical SSDF catalogue Rettura et al. (2014)

References

Ashby M. L. N. et al., 2013, The Astrophysical Journal Supplement Series, 209, 22

Bertin E., 2006, Astronomical Data Analysis Software and Systems XV ASP Conference Series, 351

Bertin E., 2011, Astronomical Data Analysis Software and Systems XX. ASP Conference Proceedings, 442

Bertin E., Arnouts S., 1996, Astronomy and Astrophysics Supplement

Bertin E., Mellier Y., Radovich M., Missonnier G., Didelon P., Morin B., 2002, Astronomical Data Analysis Software and Systems XI, 281

Bleem L. E., Stalder B., Brodwin M., Busha M. T., Gladders M. D., High F. W., Rest A., Wechsler R. H., 2014a

Bleem L. E. et al., 2014b

Bower R. G., Lucey J. R., Ellis R. S., 1992, Monthly Notices of the Royal Astronomical Society, 254

Bruzual G., Charlot S., 2003, Monthly Notices of the Royal Astronomical Society, 344, 1000

Chang C. L. et al., 2009, in The Thirteenth International Workshop on Low Temperature Detectors - LTD13. AIP Conference Proceedings, Vol. 1185, pp. 475–477

Conroy C., 2013, Annual Review of Astronomy and Astrophysics, 51, 393

Demarco R. et al., 2010, The Astrophysical Journal, 725, 1252

Demarco R. et al., 2005, Astronomy and Astrophysics, 432, 381

DePoy D. L. et al., 2008, in Ground-based and Airborne Instrumentation for Astronomy II. Edited by McLean, McLean I. S., Casali M. M., eds., Vol. 7014

Desai S. et al., 2012, The Astrophysical Journal, 757, 83

Faber S. M., 1972, Astronomy and Astrophysics, 20, 361

Freyhammer L. M., Andersen M. I., Arentoft T., Sterken C., Nø rregaard P., 2001, Experimental Astronomy, 12, 147

Gladders M. D., Yee H. K. C., 2000, The Astronomical Journal, 120, 2148

Grützbauch R., Bauer A. E., Jø rgensen I., Varela J., 2012, Monthly Notices of the Royal Astronomical Society, 423, 3652

Gwyn S. D. J., 2012, The Astronomical Journal, 143, 38

High F. W., Stubbs C. W., Rest A., Stalder B., Challis P., 2009, The Astronomical Journal, 138, 110

Hilton M. et al., 2010, The Astrophysical Journal, 718, 133

Hubble E. P., 1926, The Astrophysical Journal, 64, 321

Kravtsov A. V., Borgani S., 2012, Annual Review of Astronomy and Astrophysics, 50, 353

Lidman C. et al., 2008, Astronomy and Astrophysics, 489, 981

Lidman C. et al., 2012, Monthly Notices of the Royal Astronomical Society, 427, 550

Loubser S. I., Sánchez-Blázquez P., Sansom A. E., Soechting I. K., 2009, Monthly Notices of the Royal Astronomical Society, 398, 133

Lutz R. K., 1980, The Computer Journal, 23, 262

Muzzin A., Wilson G., Demarco R., Lidman C., Nantais J., Hoekstra H., Yee H. K. C., Rettura A., 2013, The Astrophysical Journal, 767, 39

Muzzin A. et al., 2009, The Astrophysical Journal, 698, 1934

Newman A. B., Ellis R. S., Andreon S., Treu T., Raichoor A., Trinchieri G., 2014, The Astrophysical Journal, 788, 51

Papovich C., 2008, The Astrophysical Journal, 676, 206

Pierre M., Pacaud F., Juin J. B., Melin J. B., Valageas P., Clerc N., Corasaniti P. S., 2011, Monthly Notices of the Royal Astronomical Society, 414, 1732

Rettura A. et al., 2014

Schuster M. T., Marengo M., Patten B. M., 2006, in Observatory Operations: Strategies, Silva D. R., Doxsey R. E., eds., Vol. 6270, pp. 627020–627020–11

Skrutskie M. F. et al., 2006, The Astronomical Journal, 131, 1163

Spinrad H., Taylor B. J., 1971, The Astrophysical Journal Supplement Series, 22, 445

Spitler L. R. et al., 2012, The Astrophysical Journal, 748, L21

Sunyaev R. A., Zeldovich Y. B., 1972, Comments on Astrophysics and Space Physics, 4

Taylor M. B., 2005, Astronomical Data Analysis Software and Systems XIV ASP Conference Series, 347

Tinker J., Kravtsov A. V., Klypin A., Abazajian K., Warren M., Yepes G., Gottlöber S., Holz D. E., 2008, The Astrophysical Journal, 688, 709

Tonini C., Bernyk M., Croton D., Maraston C., Thomas D., 2012, The Astrophysical Journal, 759, 43

Tran K.-V. H. et al., 2010, The Astrophysical Journal, 719, L126

van der Wel A. et al., 2014, The Astrophysical Journal, 788, 28

Voit G., 2005, Reviews of Modern Physics, 77, 207

Wilson G. et al., 2009, The Astrophysical Journal, 698, 1943